

Mathematical Modeling of Cancer–Bacterial Therapy: Analysis and Numerical Simulation via Physics-Informed Neural Networks

Ayoub Farkane^{a,b,1}, David Lassounon^{b,c,d,*,1}

^aTICLab, International University of Rabat, Rabat, 11100, Morocco

^bUniversité de Lorraine, CNRS, CRAN, F-54000 Nancy, France,

^cUniversité de Lorraine, CNRS, IECL, F-54000, Nancy, France,

^dUniv Rennes, INSA, CNRS, IRMAR-UMR 6625, F-35000, 35708, Rennes, France

ARTICLE INFO

Keywords:

Physics-informed neural networks
Reaction-diffusion systems
Tumor microenvironment
Bacterial cancer therapy
Global well-posedness
Numerical simulations
Convergence analysis

ABSTRACT

Bacterial cancer therapy exploits anaerobic bacteria's ability to target hypoxia tumor regions, yet the interactions among tumor growth, bacterial colonization, oxygen levels, immunosuppressive cytokines, and bacterial communication remain poorly quantified. We present a mathematical model of five coupled nonlinear reaction–diffusion equations in a two-dimensional tissue domain. We proved the global well-posedness of the model and identified its steady states to analyze stability. Furthermore, a physics-informed neural network (PINN) solves the system without a mesh and without requiring extensive data. It provides convergence guarantees by combining residual stability and Sobolev approximation error bounds. This results in an overall error rate of $\mathcal{O}(n^{-2} \ln^4(n) + N^{-1/2})$, which depends on the network width n and the number of collocation points N . We conducted several numerical experiments, including predicting the tumor's response to therapy. We also performed a sensitivity analysis of certain parameters. The results suggest that long-term therapeutic efficacy may require the maintenance of hypoxia regions in the tumor, or using bacteria that tolerate oxygen better, may be necessary for long-lasting tumor control.

1. Introduction

1.1. Background and Motivation of PINNs

Physics-informed neural networks (PINNs) were introduced in work [41]. They reformulate solving partial differential equations (PDEs) as minimizing a composite loss functional. This functional encodes the governing equations, initial conditions, and boundary conditions as soft constraints on a neural network. The approach offers three structural advantages over classical numerical methods. First, no spatial mesh is required: derivatives are computed exactly at any point in the domain via automatic differentiation through the network graph [38]. Second, the method is fully unsupervised: no labeled PDE solution data are needed, only collocation points drawn from the domain. Third, the same network simultaneously represents the solution at all times and all points, making temporal queries at arbitrary resolutions trivial after training.

These properties make PINNs well suited for systems of coupled, nonlinear PDEs with complex reaction terms. Classical methods often struggle with such systems. They face issues like mesh stiffness, operator splitting errors, or sensitivity to time-step size. However, the theoretical convergence of PINNs applied to nonlinear systems of PDEs has remained largely open, with rigorous results confined to linear or semi-nonlinear equations [34, 45, 9, 8]. The present paper addresses this gap for a five-species nonlinear reaction-diffusion system arising in mathematical biology.

1.2. Biological Context of Bacterial Cancer Therapy

In 2022, in the world, 20 million new cases of cancer were diagnosed, resulting in nearly 9.7 million deaths worldwide, according to the World Health Organization (WHO). By 2050, the number of new cases is expected to reach 35 million, an increase of 77% according to [46]. As a result, cancer remains a major cause of death worldwide. This disease results from the uncontrolled proliferation of tumor cells. These cells escape the normal mechanisms regulating the cell cycle and apoptosis [19], thereby promoting their survival, growth, and resistance to treatment. This behavior is closely linked to complex interactions with the tumor microenvironment (TME).

TME is a dynamic coupled ecosystem that can involve five main species: the tumor, bacteria, oxygen concentration, immunosuppressive cytokines, and quorum-sensing (QS) signaling molecules. Their interactions form a network of positive and negative feedback loops (Figure 1). The tumor cells consume oxygen, creating hypoxia niches that promote bacterial growth, particularly anaerobic bacteria. The bacteria produce QS signals that inhibit tumor proliferation. In addition, tumor stimulate the production of immunosuppressive cytokines, which, in turn, limit bacterial proliferation. Immunosuppressive Cytokines produced by tumor cells can inhibit bacterial spread in two ways. On one hand, they activate local immune cells, such as macrophages and neutrophils, which destroy bacteria. On the other hand, they modify the tumor microenvironment by increasing blood perfusion or oxygenation, making conditions less favorable for the anaerobic bacteria used in bacterial cancer therapy (BCT).

*Corresponding author

✉ ayoub.farkane@univ-lorraine.fr (A. Farkane);

david.lassounon@univ-lorraine.fr (D. Lassounon)

ORCID(s):

¹These authors contributed equally to this work.

Today, BCT uses a characteristic of tumors (the presence of hypoxia areas where conventional therapies such as chemotherapy or radiotherapy are ineffective). In these areas, therapeutic anaerobic bacteria can survive [32]. For example, bacteria such as *Salmonella* and *Clostridium novyi-NT* colonize these hypoxia areas and are activated to destroy tumors via their diffusible molecular signals (quorum-sensing (QS) effect) [21, 1]. QS molecules, *acyl-homoserine lactones* (AHL), and *autoinducer peptides* (AIP) [18], accumulate and are proportional to bacterial density, and are responsible for the destruction of cancer cells.

Modeling this dynamic system mathematically requires a nonlinear reaction-diffusion equations (PDE) to describe spatial heterogeneity among different species. This approach helps us understand interactions between tumors, oxygen, therapeutic bacteria, and tumor-induced cytokines. It also helps predict anti-cancer bacterial activity, which is the focus of our work.

1.3. Existing Mathematical Modeling

Several mathematical models of the tumor or immune system response and the role of hypoxia in bacterial therapy have been extensively studied in recent years (see e.g. [33, 32, 43, 27, 36, 2, 21, 14], and the references therein). In [32], a model of anaerobic bacterial infiltration into hypoxia areas and the effect of oxygen on their growth was studied, without accounting for the immune response or bacterial quorum sensing. Very recently, [14] proposed an ordinary differential equation model of interactions among tumors, bacteria, and chemotherapy treatment, but did not account for the immune response or QS signaling. Furthermore, in [21], an ordinary differential equation model of *Salmonella*-based cancer therapies is presented. Their work has shown that bacterial cytotoxicity alone is insufficient to treat tumors and that activating the immune system is important for effective treatment. In their model, the spatial heterogeneity of the different species (tumors, bacteria, immune response) and also interactions with tumor-derived immunosuppressive cytokines in response to bacteria are neglected. These often-overlooked biological phenomena may provide insight into the indirect effects of anti-cancer bacteria on tumor cells and into the tumor's response to their presence in its environment.

1.4. Deep Learning Approaches to Tumor Modeling

The intersection of deep learning and mathematical oncology has led to a rapidly growing body of research. However, physics-informed methods for modeling complex, multi-species tumor microenvironment remain largely unexplored. Early studies used PINNs in simple settings. For instance, in this work [42] applied PINNs to find parameters in classical scalar tumor growth ODE models, such as the Verhulst logistic and Montroll power-law equations. This work showed robustness to experimental noise. However, these models were purely temporal and spatially uniform, which limited their relevance for tumors influenced by

spatial gradients of nutrients and signaling molecules. Other studies have focused on diagnostic applications instead of mechanistic modeling. The paper [25] developed an attention-based multi-scale convolutional neural network optimized with hybrid multi-objective CAT algorithms, achieving a high accuracy in classifying bone marrow cancer cells. While this approach is highly effective, it relies entirely on data and does not include governing equations. This makes it complementary to, but fundamentally different from, physics-based tumor modeling. This framework [47] a physics-informed U-Net for dose prediction in intensity-modulated radiation therapy. Here, physical knowledge was included through structured input engineering rather than explicit PDE residual constraints. This shows that “physics-informed” methods cover a wide range of enforcement strategies. A more rigorous PDE-constrained formulation was later proposed in this paper [49]. This work combined PINNs with the Fisher–KPP reaction–diffusion equation. This study showed the clinical feasibility of PINNs for single-species tumor modeling. Most recently, the work [11] proposed a digital twin framework integrated U-Net segmentation, Chan–Vese active contour refinement, and a PINN-based reaction–diffusion solver.

Despite significant advances, one limitation remains. Most tumor response models based on PINN networks focus on a single cell population. As a result, they cannot account for interactions underlying emerging therapies. To address this, the present work proposes and analyzes a system of five coupled nonlinear reaction-diffusion on a tissue domain. This model describes tumor response to bacterial therapy, tumor oxygen consumption, tumor-secreted immunosuppressive cytokines, and quorum-sensing regulation. Unlike previous methods that treat the basic equations as soft constraints without formal guarantees, our work establishes the global well-posedness of the system via a mass-control structure. Furthermore, we identify three biologically relevant steady-states. In addition, we formally provide the suitability analysis for PINN approximation for considered system, including approximation error estimates.

1.5. Contributions

This paper makes the following four contributions.

1. **A coupled reaction-diffusion system for BCT.** We formulate and described system (8), coupling tumor density response with quorum-sensing inhibition, hypoxia-activated bacterial growth (by a inverse Michaelis–Menten function), vascular oxygen exchange, tumor-induced immunosuppressive cytokines production in response to bacteria (see Section 2). The system is the first to simultaneously integrate these cross-interactions.
2. **Well-posedness and steady-states analysis.** Under general assumptions (H) on initial data and system parameters in (8), we prove the following: The global existence, uniqueness, regularity, and positivity of a bounded solution in an appropriate Sobolev space (see Theorem 3.1 and Proposition 3.1, Section 3). We also

provide a steady-state stability analysis and show that no Turing instability is induced by diffusion. Details are provided in Section 3.

3. **PINN convergence analysis for our system.** We establish convergence guarantees for the proposed PINN applied to the system (8). Specifically, our analysis includes: (i) a Lipschitz bound on the nonlinear operator (Lemma 5.1); (ii) a stability theorem (Theorem 5.1) relating approximation error to the network residual via energy estimates; (iii) an approximation theorem (Theorem 5.2); and (iv) a generalization bound (Lemma 5.2) for the discrete loss. Finally, Theorem 5.3 combines these results to characterize how the method converges as a function of the network architecture and the total number of collocation points.
4. **Numerical simulations.** We validate the proposed framework with numerical simulations. We conducted various experiments to analyse the different behaviors of solutions. They show that the network describes the complex nonlinear dynamics of the underlying biological system with high precision and does not rely on synthetic or assumed parameter values. Simulations confirm the expected interactions between the system components, that are illustrated in Figure 1.

The rest of the article is organized as follows. Section 2 formulates the mathematical model (8). Section 3 presents the mathematical analysis, including the well-posedness theorem with a complete proof and the steady-state characterization. Section 4 develops the PINN framework for the considered system. Section 5 proves the convergence theorems for the applied PINNs and discusses parameter calibration. Section 6 presents validation results from various numerical experiments. Finally, Section 7 discusses limitations and perspectives.

2. Mathematical Modeling

2.1. Evolution of Tumor Density under Treatment

Mathematical modeling of tumor evolution under therapy (chemotherapy, immunotherapy, radiotherapy, etc.) has been intensively studied in recent years (see e.g. [10, 5, 23, 22, 35, 31, 28, 29] and the references therein). Its value lies particularly in understanding the dynamic mechanisms of growth, resistance, and response to treatment. The tumor response model adopted here describes the indirect action of anticancer bacteria in tumor cells density T in the tissue via diffusible molecular signals S released by bacteria. We consider the following reaction diffusion equation:

$$\begin{aligned} \frac{\partial T}{\partial t}(t, x) = & D_T \Delta T(t, x) + \rho_T T(t, x) \left(1 - \frac{T(t, x)}{c}\right) \\ & - \delta_T T(t, x) - \alpha_S S(t, x) T(t, x) \text{ in } \mathcal{Q} = (0, \tau) \times \Omega. \end{aligned} \quad (1)$$

In equation (1), D_T is the diffusion coefficient of tumor cells in tissue. The second term in the second member of

the equation represents the standard term describing tumor cell proliferation, characterized by an intrinsic proliferation rate ρ_T and limited by the maximum capacity of the microenvironment c [21]. The term $-\delta_T T$ is natural mortality due to apoptosis or necrosis. The last term $-\alpha_S S T$ reflects the influence of the diffusible bacterial signal S on the tumor population. It describes the indirect and regulated cytotoxicity of bacteria. The higher the concentration of S , the greater the inhibition of tumor cells. The coefficient δ_T is the degradation rate, and α_S represents the efficacy of the cytotoxic action of the diffusible bacterial signal S . The set $\Omega \subset \mathbb{R}^d$ ($d = 1, 2, 3$) is open bounded represents a tissue, whose boundary $\partial\Omega$ is sufficiently regular. The parameter $\tau > 0$ is the final time horizon. The quantity $T(t, x)$ is the tumor density at time $t \in (0, \tau)$ and position $x \in \Omega$.

2.2. Evolution of Bacterial Density

The evolution of bacterial density B in tumor tissue is modeled by taking into account their spatial diffusion, their proliferation controlled by oxygen availability O , their natural mortality, and their elimination by immunosuppressive cytokines I present in the microenvironment. We consider the following equation:

$$\begin{aligned} \frac{\partial B}{\partial t}(t, x) = & D_B \Delta B(t, x) + \rho_B B(t, x) \frac{K_H}{K_H + O(t, x)} \\ & - \delta_B B(t, x) - \beta_I I(t, x) B(t, x) \text{ in } \mathcal{Q}. \end{aligned} \quad (2)$$

The model (2) combines several key biological processes. The quantity $B(t, x)$ is the bacterial density at time $t \in (0, \tau)$ and position $x \in \Omega$. The term $D_B \Delta B$ represents the spatial diffusion of bacteria in tumor tissue. The coefficient ρ_B is the bacterial proliferation rate. The bacterial growth is described by the term $\rho_B B K_H / (K_H + O(t, x))$. In this term, the quantity $K_H / (K_H + O(t, x))$ reflects the preference of bacteria for hypoxia conditions. In areas with high oxygen concentrations, there is low bacterial growth. For example, therapeutic bacteria such as *Salmonella Typhimurium* or *Clostridium novyi*-NT germinate and proliferate in hypoxia regions [50, 44]. The term $-\delta_B B$ corresponds to the natural mortality of bacteria with the mortality rate δ_B . The term $-\beta_I I B$ models bacterial elimination by immunosuppressive cytokines $I(x, t)$ with β_I the efficiency of the immunosuppressive response. The constant D_B is the diffusion coefficient of bacteria, and ρ_B is the bacterial proliferation rate. The constant K_H is the oxygen inhibition constant.

2.3. Evolution of Oxygen Density

The evolution of oxygen concentration, denoted as $O(x, t)$, in tissues is described by a diffusion-consumption model (3) that includes an external oxygen [32, 33]. This model reflects how oxygen diffuses through tissue, is consumed by tumor cells, and is replenished from the surrounding vascular environment. It provides a framework for representing the spatiotemporal dynamics of hypoxia, which is a crucial factor in tumor growth and bacterial colonization. For the oxygen concentration in tissues, we consider the following

equation:

$$\frac{\partial O}{\partial t} = D_O \Delta O(t, x) - \gamma_T T(t, x) O(t, x) + \gamma_{vas} (O_{vas} - O(t, x)) \text{ in } \mathcal{Q}. \quad (3)$$

The equation (3) describes the classical processes that govern oxygen distribution within the tumor region. The term $D_O \Delta O$ represents the spatial diffusion of oxygen through the tissue, where D_O is the diffusion coefficient that depends on the medium's structure and its porosity. The terms $-\gamma_T T O$ represents the consumption of oxygen by tumor cells. The multiplicative form of these terms indicates that oxygen consumption increases with cell density and local oxygen availability. The coefficients γ_T represent the consumption rate. The term $\gamma_{vas} (O_{vas} - O(t, x))$ accounts for the external oxygen supply from the vascular environment. The parameter γ_{vas} controls the rate at which the local oxygen concentration approaches the reference value O_{vas} . The value of O_{vas} represents the vascular irrigation. Including an explicit term representing internal vascular oxygen supply is essential for accurately modeling oxygen distribution within the tumor. It enables a proper balance between diffusion, cellular consumption, and the limited contribution of blood perfusion. Without such a term, oxygen gradients would be underestimated, resulting in an inadequate representation of hypoxia regions.

2.4. Evolution of Immunosuppressive Cytokines Density

The evolution of the density of immunosuppressive cytokines, denoted $I(x, t)$, in the TME is described by a reaction-diffusion equation (4) inspired by the work of [21]. The equation describes the biological process by which tumor cells produce immunosuppressive cytokines to evade therapies. Secreted by tumor cells, these cytokines, such as TGF- β and IL-10, diffuse into surrounding tissues to establish an immunosuppressive tumor microenvironment and naturally degrade. Together, they control inflammation, angiogenesis, and tumor cell survival [48, 40, 19]. For example, cytokines IL-10 and TNF- α activate the NF- κ B signaling pathway, contributing to inflammation and tumor progression. Their evolution is described by the following equation

$$\frac{\partial I}{\partial t}(t, x) = D_I \Delta I(t, x) + \beta_T T(t, x) - \delta_I I(t, x) \text{ in } \mathcal{Q}. \quad (4)$$

The model describes the distribution of tumor immunosuppressive cytokines in the tissue. The term $D_I \Delta I$ represents the spatial diffusion of cytokines through the tissue, where D_I is the diffusion coefficient. The term $\beta_T T$ represents cytokines production by tumor cells. This production is proportional to the local density of tumor cells and reflects tumor-induced immune activation. The term $-\delta_I I$ represents the spontaneous degradation of cytokines, taking into account their half-life and elimination by consumption by other immune cells. By combining these terms, the model allows for the consideration of spatial gradients and the

temporal evolution of immunosuppressive cytokines. This approach is essential for representing inhibitory effects on bacterial growth. Consequently, (4) enables the investigation of immune feedback on both bacteria and tumor.

2.5. Evolution of Diffusible Bacterial Signals

As explained in the first part of the introduction, the integration of diffusible bacterial molecular signals represented by S acting on tumor dynamics allows us to understand microbial communication, such as the *quorum-sensing* ([3]) on the viability of cancer cells. These signals can be *acyl-homoserine lactones* (AHLs) or *autoinducing peptides* (AIPs) [18]. The dynamics of the diffusible bacterial signal $S(x, t)$ in time and space are described by a diffusion-production-degradation model given by the equation (5). This model shows how the signal diffuses through tissue, is produced by bacteria, and degrades naturally. It shows the influence of bacterial signals of tumor viability carried by the term $-\alpha_S S T$ in the tumor equation (1). We consider the following equation:

$$\frac{\partial S}{\partial t}(t, x) = D_S \Delta S(t, x) + \beta_B B(t, x) - \delta_S S(t, x) \text{ in } \mathcal{Q}. \quad (5)$$

The term $D_S \Delta S$ refers to the spatial diffusion of the signal within the tissue, where D_S is the diffusion coefficient. The term $\beta_B B$ models the production of the signal by bacteria, with β_B the production parameter. Meanwhile, the term $-\delta_S S$ accounts for the natural degradation of the signal in the tissue, where δ_S is the degradation coefficient. The *quorum-sensing* mechanism plays an essential role in the collective coordination of bacteria within the tumor microenvironment. Bacteria produce and release a diffusible molecular signal into the environment, the concentration of which increases with bacterial density. When this concentration exceeds a certain threshold, it triggers the expression of specific genes linked to virulence, cytotoxicity, or the production of anti-cancer enzymes. This approach makes (5) more consistent with experimental observations of bacterial therapies using *quorum-sensing* strains (e.g., *Salmonella* in [21] and *Pseudomonas* in [37]). In the literature, mathematical modeling of molecular signals of bacteria is often neglected. Their explicit inclusion highlights their diffuse local interactions with the tumor.

The Figure 1 presents a simplified diagram of the main interactions between variables. The arrows indicate the influences (positive in green, negative in red) deduced from the reaction terms of the equations (without diffusion). The nodes represent only the variables T (tumor), B (bacteria), O (oxygen), I (immunosuppressive cytokines), S (signal). Tumor cells consume oxygen ($T \rightarrow O$), which promotes hypoxia and stimulates bacterial growth ($O \rightarrow B$). Bacteria produce a cytotoxic diffusible signal ($B \rightarrow S \rightarrow T$) that inhibits tumor proliferation. The tumor also induces the production of immunosuppressive cytokines ($T \rightarrow I$), which exert an inhibitory effect on bacteria ($I \rightarrow B$), thus forming a network of negative and positive feedback loops. This interaction describes the combined effects of hypoxia, bacterial cytotoxicity, and the immune response on the tumor.

In this paper, we will consider the following initial conditions, e.g., respectively the initial tumor density, bacterial density, oxygen concentration, immunosuppressive cytokines concentration, and the diffusible bacterial signals at initial time $t = 0$ and for all $x \in \Omega$:

$$\begin{aligned} T(0, x) &= T_0(x), B(0, x) = B_0(x), O(0, x) = O_0(x), \\ I(0, x) &= I_0(x), S(0, x) = S_0(x) \text{ in } \Omega, \end{aligned} \quad (6)$$

with homogeneous Neumann boundary conditions as follows

$$\frac{\partial T}{\partial n} = \frac{\partial B}{\partial n} = \frac{\partial O}{\partial n} = \frac{\partial I}{\partial n} = \frac{\partial S}{\partial n} = 0 \text{ on } \Sigma := (0, \tau) \times \partial\Omega. \quad (7)$$

where the vector n is the outward normal to $\partial\Omega$.

By combining equations (1)-(2)-(3)-(4)-(5)-(6)-(7), we obtain the following interactive system of diffusion reaction equations:

$$\left\{ \begin{aligned} \frac{\partial T}{\partial t}(t, x) &= D_T \Delta T(t, x) + \rho_T T(t, x) \left(1 - \frac{T(t, x)}{c}\right) \\ &\quad - \delta_T T(t, x) - \alpha_S S(t, x) T(t, x) \text{ in } Q, \\ \frac{\partial B}{\partial t}(t, x) &= D_B \Delta B(t, x) + \rho_B B(t, x) \frac{K_H}{K_H + O(t, x)} \\ &\quad - \delta_B B(t, x) - \beta_I I(t, x) B(t, x) \text{ in } Q, \\ \frac{\partial O}{\partial t}(t, x) &= D_O \Delta O(t, x) - \gamma_T T(t, x) O(t, x) \\ &\quad + \gamma_{vas} (O_{vas} - O(t, x)) \text{ in } Q, \\ \frac{\partial I}{\partial t}(t, x) &= D_I \Delta I(t, x) + \beta_T T(t, x) - \delta_I I(t, x) \text{ in } Q, \\ \frac{\partial S}{\partial t}(t, x) &= D_S \Delta S(t, x) + \beta_B B(t, x) - \delta_S S(t, x) \text{ in } Q, \\ \frac{\partial T}{\partial n} = \frac{\partial B}{\partial n} = \frac{\partial O}{\partial n} = \frac{\partial I}{\partial n} = \frac{\partial S}{\partial n} &= 0 \text{ on } \Sigma, \\ T(0, x) &= T_0(x), B(0, x) = B_0(x), O(0, x) = O_0(x), \\ I(0, x) &= I_0(x), S(0, x) = S_0(x) \text{ in } \Omega. \end{aligned} \right. \quad (8)$$

The system (8) describes the simultaneous evolution of biological variables T, B, O, I, S , representing tumor density, bacterial density, oxygen concentration, immune cytokine concentration, and diffusible signal concentration, respectively. It formalizes the cross-feedback loops that govern the balance between tumor cell proliferation and destruction, particularly under the effect of hypoxia and bacterial *quorum-sensing* mechanisms. This coupling provides a better representation of the complex dynamics of the tumor microenvironment under bacterial therapy. The mathematical analysis of system (8) will be discussed in the following section.

3. Mathematical Analysis

3.1. Existence and Uniqueness of Global Classical Solutions

In this section, we state and prove the existence, uniqueness, and regularity of global classical solutions of the system (8). Before that, we make the following assumptions, which we assume hold throughout the paper.

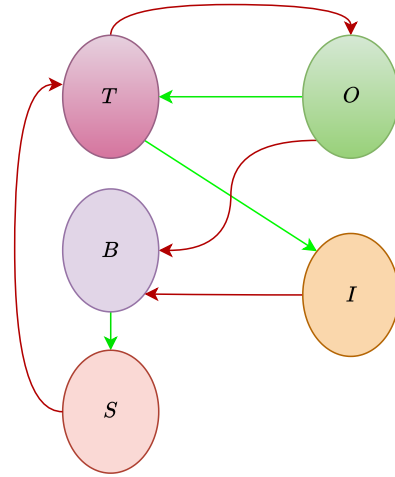


Figure 1: Simplified diagram of the main interactions variables T, B, O, I, S .

General assumptions 3.1. (H) : We assume that the initial data $(T_0, B_0, O_0, I_0, S_0) =: \mathbf{U}_0 \in (L^\infty(\Omega)_+ \cap H^1(\Omega))^5$. The real diffusion coefficients D_T, D_B, D_O, D_I, D_S are non-negative, and the real proliferation, degradation, and consumption coefficients $\rho_T, \rho_B, \beta_B, \beta_T, \beta_I, \delta_T, \delta_B, \delta_I, \delta_S, \alpha_S, \gamma_T, \gamma_{vas}, K_H, O_{vas}$ are non-negative.

Throughout, we denote by C a generic positive constant whose exact value is not important and may vary from line to line.

Now, we collect some known definitions of a classical solution of (8). For more details, we refer the reader to [39].

Definition 3.1. The classical solution to (8) on $[0, \tau]$, is a function $\mathbf{U} := (T, B, O, I, S)^\top : [0, \tau] \times \Omega \rightarrow \mathbb{R}^5$ such that

$$\mathbf{U} \in C([0, \tau]; (L^1(\Omega))^5) \cap (L^\infty([0, \tau - \tau^*] \times \Omega))^5, \forall \tau^* \in (0, \tau),$$

and for all $k, l = 1, \dots, N$ and all $p \in [1, \infty)$,

$$\partial_t \mathbf{U}, \partial_{x_k} \mathbf{U}, \partial_{x_k x_l} \mathbf{U} \in (L^p((\tau^*, \tau - \tau^*) \times \Omega))^5,$$

and the equations in (37) are satisfied a.e..

Let the function $F = (F_1, \dots, F_5) \in \mathbb{R}^5$. We say that F is *quasi-positive* if it satisfies the following property:

$$\begin{aligned} \forall r \in ([0, +\infty))^5, \forall i = 1, \dots, 5, \\ F_i(r_1, \dots, r_{i-1}, 0, r_{i+1}, \dots, r_m) \geq 0, \end{aligned} \quad (9)$$

where we denote $r = (r_1, \dots, r_5)$.

We say that F satisfies a *mass-control structure* if there exists a constant $C > 0$, a vector $\mathbf{b} \in \mathbb{R}^5$, and a lower triangular invertible 5×5 matrix \mathbf{P} with nonnegative entries such that

$$\forall r \in ([0, +\infty))^5, \quad \mathbf{P}F(r) \leq C \left[1 + \sum_{i=1}^5 r_i \right] \mathbf{b}. \quad (10)$$

Lemma 3.1. The nonlinearity $F = (F_T, F_B, F_O, F_I, F_S)^\top$ from (8) with $U = (T, B, O, I, S)^\top \geq 0$ componentwise and

$$\begin{aligned} F_T(U) &= \rho_T T \left(1 - \frac{T}{c}\right) - \delta_T T - \alpha_S S T; \\ F_B(U) &= \rho_B B \frac{K_H}{K_H + O} - \delta_B B - \beta_I I B; \\ F_O(U) &= -\gamma_T T O + \gamma_{vas} (O_{vas} - O); \\ F_I(U) &= \beta_T T - \delta_I I; \\ F_S(U) &= \beta_B B - \delta_S S, \end{aligned} \quad (11)$$

is quasi-positive and satisfies the mass-control structure.

Proof 1. Let $U = (T, B, O, I, S)^\top \geq 0$ componentwise, we have

$$\begin{aligned} F_T(0, B, O, I, S) &= 0 \geq 0; \\ F_B(T, 0, O, I, S) &= 0 \geq 0; \\ F_O(T, B, 0, I, S) &= \gamma_{vas} O_{vas} \geq 0; \\ F_I(T, B, O, 0, S) &= \beta_T T \geq 0; \\ F_S(T, B, O, I, 0) &= \beta_B B \geq 0. \end{aligned} \quad (12)$$

Then, according to (9), $F = (F_T, F_B, F_O, F_I, F_S)^\top$ is quasi-positive. Moreover, for all $U = (T, B, O, I, S)^\top \geq 0$ componentwise, we have $K_H/(K_H + O) \leq 1$ and that

$$\begin{aligned} F_T(U) + F_B(U) + F_O(U) + F_I(U) + F_S(U) \\ \leq \rho_T T + \rho_B B + \gamma_{vas} O_{vas} + \beta_T T + \rho_B B \\ \leq C(1 + T + B) \\ \leq C(1 + T + B + O + I + S), \end{aligned} \quad (13)$$

implies that $F = (F_T, F_B, F_O, F_I, F_S)^\top$ satisfies the mass-control structure in the sense of (10) for $\mathbf{P} = \text{diag}(1, 1, 1, 1, 1)$ and $\mathbf{b} = (1, 1, 1, 1, 1)^\top$.

The existence of global classical solutions of (8) is given by the following

Theorem 3.1. The system (8) has a unique global classical solution $\mathbf{U} = (T, B, O, I, S)^\top \in (L^\infty(Q)_+)^5$ corresponding to the initial data $\mathbf{U}_0 = (T_0, B_0, O_0, I_0, S_0)^\top \in (L^\infty(\Omega)_+)^5$ in the sense of Definition 3.1.

Proof 2. The global well-posedness of (8) is demonstrated using a more general framework presented in [39, Lemma 1.1 and Theorem 3.5]. Before applying this result, we prove that our system (8) fits well within this framework by showing that for all $U = (T, B, O, I, S)^\top \geq 0$ componentwise, the nonlinear operator $F(U)$ satisfies [39, conditions (P) and (M)] given by conditions (9) and (10). Indeed, the nonlinearity F has at most polynomial and of class $C^1([0, \infty)^5; \mathbf{R}^5)$. By Lemma (3.1), F satisfies the quasi-positivity condition and admits a mass-control structure. Then, by [39, Lemma 1.1 and Theorem 3.5], for any initial data $\mathbf{U}_0 = (T_0, B_0, I_0, S_0)^\top \in (L^\infty(\Omega)_+)^5$, the system (8) admits a unique classical global solution $\mathbf{U} = (T, B, O, I, S)^\top \in (L^\infty(Q)_+)^5$.

Since from (H), we have more regularity on the initial data \mathbf{U}_0 , we then demonstrate that the unique corresponding global classical solution satisfies the regularities given in the following

Proposition 3.1. The global classical solution \mathbf{U} to (8) corresponding to the initial data $\mathbf{U}_0 \in (L^\infty(\Omega)_+ \cap H^1(\Omega))^5$ satisfies

$$\begin{aligned} \mathbf{U} &\in C([0, \tau]; (L^2(\Omega))^5) \cap (L^\infty(0, \tau; H^1(\Omega)))^5, \\ \mathbf{U} &\in (L^2(0, \tau; H^2(\Omega)) \cap H^1(0, \tau; L^2(\Omega)))^5. \end{aligned} \quad (14)$$

such that for all $t \in (0, \tau)$,

$$\begin{aligned} \|\mathbf{U}(t)\|_{(L^2(\Omega))^5}^2 + 2d_0 \int_0^t \|\nabla \mathbf{U}(s)\|_{(L^2(\Omega))^5}^2 ds \\ \leq C \|\mathbf{U}_0\|_{(L^2(\Omega))^5}^2, \end{aligned} \quad (15)$$

$$\begin{aligned} \|\nabla \mathbf{U}(t)\|_{(L^2(\Omega))^5}^2 + d_0 \int_0^t \|\Delta \mathbf{U}(s)\|_{(L^2(\Omega))^5}^2 ds \\ \leq C \|\nabla \mathbf{U}_0\|_{(L^2(\Omega))^5}^2, \end{aligned} \quad (16)$$

where $d_0 := \min(D_T, D_B, D_O, D_I, D_S) > 0$.

Proof 3. Since $\mathbf{U}_0 \in (L^\infty(\Omega)_+ \cap H^1(\Omega))^5 \subset (L^\infty(\Omega)_+)^5$, then according to Theorem 3.1, the system (8) admits a unique global classical solution $\mathbf{U} \in (L^\infty(Q)_+)^5$. Then, \mathbf{U} verifies the following abstract form of (8).

$$\begin{cases} \frac{\partial \mathbf{U}}{\partial t} + \mathbf{A} \mathbf{U} = \mathbf{F}(\mathbf{U}) \text{ in } Q, \\ \partial_n \mathbf{U} = 0_{\mathbb{R}^5} \text{ in } \Sigma, \\ \mathbf{U}(0, x) = \mathbf{U}_0(x) \text{ in } \Omega, \end{cases} \quad (17)$$

where $\mathbf{A} = -\mathbf{D} \Delta$ with $\mathbf{D} = \text{diag}(D_T, D_B, D_O, D_I, D_S)$, and the nonlinearity $F = (F_T, F_B, F_O, F_I, F_S)$ define in (11). We have:

$$\begin{aligned} (\mathbf{F}(\mathbf{U}), \mathbf{U})_{(L^2(\Omega))^5} &= \int_\Omega F_T(\mathbf{U}) T dx + \int_\Omega F_B(\mathbf{U}) B dx \\ &+ \int_\Omega F_O(\mathbf{U}) O dx + \int_\Omega F_I(\mathbf{U}) I dx \\ &+ \int_\Omega F_S(\mathbf{U}) S dx. \end{aligned} \quad (18)$$

We will estimate each of the five terms of (18). For the first term, using the fact that $T \geq 0$ since $\mathbf{U} \geq 0$ componentwise, we have

$$\begin{aligned} \int_\Omega F_T(\mathbf{U}) T dx &= \int_\Omega \rho_T T^2 \left(1 - \frac{T}{c}\right) - \delta_T T^2 - \alpha_S S T^2 dx \\ &\leq C \|T\|_{L^2(\Omega)}^2. \end{aligned} \quad (19)$$

For the second term of (18), using $\mathbf{U} \geq 0$ then, we have $K_H/(K_H + O) \leq 1$ and that

$$\begin{aligned} \int_\Omega F_B(\mathbf{U}) B dx &= \int_\Omega \left(\rho_B B^2 \frac{K_H}{K_H + O} - \delta_B B^2 - \beta_I I B^2\right) \\ &\leq C \|B\|_{L^2(\Omega)}^2. \end{aligned} \quad (20)$$

Similarly to the first two estimates, using the fact that $\mathbf{U} \geq 0$, and Hölder's and Young's inequality, we obtain

$$\begin{aligned} \int_{\Omega} F_O(\mathbf{U})O \, dx &= \int_{\Omega} (-\gamma_T T O^2 + \gamma_{vas}(O_{vas}O - O^2)) \\ &\leq \gamma_{vas} \int_{\Omega} O_{vas}O \, dx \\ &\leq C(1 + \|O\|_{L^2(\Omega)}^2). \end{aligned} \quad (21)$$

For the penultimate term, applying Hölder's and Young's inequality, we have

$$\begin{aligned} \int_{\Omega} F_I(\mathbf{U})I \, dx &= \int_{\Omega} (\beta_T T I - \delta_I I^2) \, dx \\ &\leq \beta_I \|T\|_{L^2(\Omega)} \|I\|_{L^2(\Omega)} \\ &\leq C(\|T\|_{L^2(\Omega)}^2 + \|I\|_{L^2(\Omega)}^2), \end{aligned} \quad (22)$$

and that

$$\begin{aligned} \int_{\Omega} F_S(\mathbf{U})S \, dx &= \int_{\Omega} (\beta_B B S - \delta_S S^2) \, dx \\ &\leq C(\|B\|_{L^2(\Omega)}^2 + \|S\|_{L^2(\Omega)}^2). \end{aligned} \quad (23)$$

By summing all estimates (19), (20), (21), (22), (23), we obtain

$$(\mathbf{F}(\mathbf{U}), \mathbf{U})_{L^2(\Omega)^5} \leq C \left(1 + \|\mathbf{U}\|_{L^2(\Omega)^5}^2\right). \quad (24)$$

Now, taking the inner product of the first equation of (17) by \mathbf{U} and using Definition 3.1, we have

$$\begin{aligned} \langle \partial_t \mathbf{U}(t), \mathbf{U}(t) \rangle + (\mathbf{D}\nabla \mathbf{U}(t), \nabla \mathbf{U}(t))_{(L^2(\Omega))^5} \\ = (\mathbf{F}(\mathbf{U}(t)), \mathbf{U}(t))_{(L^2(\Omega))^5}, \end{aligned} \quad (25)$$

where $\langle \cdot, \cdot \rangle$ denotes the duality bracket between $((H^1(\Omega)^5))'$ and $(H^1(\Omega))^5$, and $(\cdot, \cdot)_{(L^2(\Omega))^5}$ is the inner product in $(L^2(\Omega))^5$.

Setting $d_0 := \min(D_T, D_B, D_O, D_I, D_S) > 0$ integrating (25) over $[0, t]$ for all $t \in (0, \tau)$:

$$\begin{aligned} \frac{1}{2} \|\mathbf{U}(t)\|_{(L^2(\Omega))^5}^2 - \frac{1}{2} \|\mathbf{U}_0\|_{(L^2(\Omega))^5}^2 \\ + d_0 \int_0^t \|\nabla \mathbf{U}(s)\|_{(L^2(\Omega))^5}^2 \, ds \\ \leq \int_0^t (\mathbf{F}(\mathbf{U}(s)), \mathbf{U}(s))_{(L^2(\Omega))^5} \, ds \end{aligned} \quad (26)$$

According to (24), we have for all $t \in (0, \tau)$:

$$\begin{aligned} \frac{1}{2} \|\mathbf{U}(t)\|_{(L^2(\Omega))^5}^2 - \frac{1}{2} \|\mathbf{U}_0\|_{(L^2(\Omega))^5}^2 \\ + d_0 \int_0^t \|\nabla \mathbf{U}(s)\|_{(L^2(\Omega))^5}^2 \, ds \\ \leq C \int_0^t \left(1 + \|\mathbf{U}(s)\|_{(L^2(\Omega))^5}^2\right) \, ds. \end{aligned} \quad (27)$$

Form the Grönwall's Lemma, we have

$$\begin{aligned} \|\mathbf{U}(t)\|_{(L^2(\Omega))^5}^2 + 2d_0 \int_0^t \|\nabla \mathbf{U}(s)\|_{(L^2(\Omega))^5}^2 \, ds \\ \leq C \|\mathbf{U}_0\|_{(L^2(\Omega))^5}^2. \end{aligned} \quad (28)$$

Then,

$$\mathbf{U} \in L^\infty(0, \tau; (L^2(\Omega))^5) \cap (L^2(0, \tau; H^1(\Omega)))^5.$$

Moreover, since $\mathbf{D}\Delta \mathbf{U} \in (L^2(0, \tau; (H^1(\Omega))'))^5$ (because $\mathbf{U} \in (L^2(0, \tau; H^1(\Omega)))^5$ and $\mathbf{F}(\mathbf{U}) \in (L^2(0, \tau; (H^1(\Omega))'))^5$ (arguing as in (24) with test functions in $(H^1(\Omega))^5$), then $\partial_t \mathbf{U} = \mathbf{D}\Delta \mathbf{U} + \mathbf{F}(\mathbf{U}) \in (L^2(0, \tau; (H^1(\Omega))'))^5$. Therefore, according to Aubin–Lions Lemma [30], $\mathbf{U} \in C([0, \tau]; (L^2(\Omega))^5)$.

Thus,

$$\mathbf{U} \in C([0, \tau]; (L^2(\Omega))^5) \cap (L^2(0, \tau; H^1(\Omega)))^5. \quad (29)$$

For the other results regularities of \mathbf{U} , let us first estimate $\mathbf{F}(\mathbf{U})$ in the $(L^2(\Omega))^5$ norm. We note that

$$\begin{aligned} \|\mathbf{F}(\mathbf{U})\|_{(L^2(\Omega))^5}^2 &= \|F_T(\mathbf{U})\|_{L^2(\Omega)}^2 + \|F_B(\mathbf{U})\|_{L^2(\Omega)}^2 \\ &\quad + \|F_O(\mathbf{U})\|_{L^2(\Omega)}^2 + \|F_I(\mathbf{U})\|_{L^2(\Omega)}^2 \\ &\quad + \|F_S(\mathbf{U})\|_{L^2(\Omega)}^2. \end{aligned} \quad (30)$$

Taking the square term by term in (13), and integrating over Ω , we have

$$\|\mathbf{F}(\mathbf{U})\|_{(L^2(\Omega))^5}^2 \leq C \left(1 + \|\mathbf{U}\|_{(L^2(\Omega))^5}^2\right). \quad (31)$$

Taking the inner product of the first equation of (17) with $-\Delta \mathbf{U}$, integrating over Ω , using (31), Hölder's, and Young's inequality, we obtain for all $\varepsilon > 0$:

$$\begin{aligned} \frac{1}{2} \frac{d}{dt} \|\nabla \mathbf{U}\|_{(L^2(\Omega))^5}^2 + d_0 \|\Delta \mathbf{U}\|_{(L^2(\Omega))^5}^2 \\ \leq \|\mathbf{F}(\mathbf{U})\|_{(L^2(\Omega))^5} \|\Delta \mathbf{U}\|_{(L^2(\Omega))^5} \\ \leq C_\varepsilon \|\mathbf{F}(\mathbf{U})\|_{(L^2(\Omega))^5}^2 + \varepsilon \|\Delta \mathbf{U}\|_{(L^2(\Omega))^5}^2 \\ \leq C_\varepsilon (1 + \|\mathbf{U}\|_{(L^2(\Omega))^5}^2) + \varepsilon \|\Delta \mathbf{U}\|_{(L^2(\Omega))^5}^2. \end{aligned} \quad (32)$$

By choosing $\varepsilon = \frac{d_0}{2}$, and using a nonlinear Grönwall Lemma, we have for all $t \in (0, \tau^*)$:

$$\|\nabla \mathbf{U}(t)\|_{(L^2(\Omega))^5}^2 + d_0 \int_0^t \|\Delta \mathbf{U}(s)\|_{(L^2(\Omega))^5}^2 \, ds \leq C \|\nabla \mathbf{U}_0\|_{(L^2(\Omega))^5}^2. \quad (33)$$

This implies that

$$\mathbf{U} \in (L^\infty(0, \tau; H^1(\Omega)) \cap L^2(0, \tau; H^2(\Omega)))^5. \quad (34)$$

According to (31), and since $\mathbf{U} \in (L^2(\Omega))^5$, we have $\mathbf{F}(\mathbf{U}) \in (L^2(\Omega))^5$. Moreover, since $\mathbf{U} \in (L^2(0, \tau; H^2(\Omega)))^5$, it follows that $\mathbf{D}\Delta \mathbf{U} \in (L^2(\Omega))^5$. Therefore, we obtain

$$\partial_t \mathbf{U} = \mathbf{D}\Delta \mathbf{U} + \mathbf{F}(\mathbf{U}) \in (L^2(\Omega))^5. \quad (35)$$

Therefore, the estimates and regularity results (29), (34), (35), (28), and (33) complete the proof of Proposition 3.1.

Remark 3.1. We used a homogeneous Neumann boundary condition for all variables T, B, O, I, S in (7) to maintain a clear mathematical and numerical framework for analyzing system (8). In our future work, we may consider other boundary conditions for some of the five variables, as in [28, 29], where a nonlinear term is used at the boundary to model tumor invasion into other organs.

3.2. Nondimensionalization of the system

In order to introduce dimensionless variables, we consider the following rescalings:

$$\begin{aligned} \tilde{t} &= \rho_T t; \quad \tilde{x} = \frac{x}{L}; \quad L = \sqrt{\frac{D_T}{\rho_T}}; \quad \tilde{T} = \frac{T}{c}; \quad \tilde{B} = \frac{B}{B_*}; \\ \tilde{O} &= \frac{O}{O_{vas}}; \quad \tilde{I} = \frac{I}{I_*}; \quad \tilde{S} = \frac{S}{S_*}; \quad I_* = \frac{\beta_T c}{\rho_T}; \quad S_* = \frac{\beta_B B_*}{\rho_T}. \end{aligned} \quad (36)$$

By replacing t, x, T, B, O, I, S obtained by (36) in (8), we have in $\tilde{\Omega} =: \Omega/L$, the following dimensionless system (for simplicity, the tildes are omitted):

$$\begin{cases} \partial_t T = \Delta T + T(1-T) - t_0 T - \alpha_0 S T, \\ \partial_t B = d_B \Delta B + \mu_0 B \frac{\kappa}{\kappa + O} - b_0 B - \beta_0 I B, \\ \partial_t O = d_O \Delta O - \gamma_0 T O + \varrho_0(1-O), \\ \partial_t I = d_I \Delta I + T - \eta_0 I, \\ \partial_t S = d_S \Delta S + B - \lambda_0 S, \\ \partial_n T = \partial_n B = \partial_n O = \partial_n I = \partial_n S = 0 \text{ on } \Sigma, \\ T(0, x) = T_0(x); \quad B(0, x) = B_0(x); \\ O(0, x) = O_0(x); \quad I(0, x) = I_0(x); \quad S(0, x) = S_0(x), \end{cases} \quad (37)$$

where the dimensionless parameters are given by

$$\begin{aligned} d_B &= \frac{D_B}{D_T}; \quad d_O = \frac{D_O}{D_T}; \quad d_I = \frac{D_I}{D_T}; \quad d_S = \frac{D_S}{D_T}; \quad \mu_0 = \frac{\rho_B}{\rho_T}; \\ t_0 &= \frac{\delta_T}{\rho_T}; \quad b_0 = \frac{\delta_B}{\rho_T}; \quad \eta_0 = \frac{\delta_I}{\rho_T}; \quad \lambda_0 = \frac{\delta_S}{\rho_T}; \quad \alpha_0 = \frac{\alpha_S S_*}{\rho_T}; \\ \beta_0 &= \frac{\beta_I I_*}{\rho_T}; \quad \gamma_0 = \frac{\gamma_T c}{\rho_T}; \quad \varrho_0 = \frac{\gamma_{vas}}{\rho_T}; \quad \kappa = \frac{K_H}{O_{vas}}. \end{aligned} \quad (38)$$

3.3. Homogeneous steady states analysis

In this subsection, we consider the system (37) omitting spatial dependence in order to study spatially homogeneous steady states. The Theorem 3.1 guaranteed that the solution of system (37) is positive and bounded. The following proposition give the spatially homogeneous steady states and their positivity conditions

Proposition 3.2. The system (37) admits three spatially homogeneous stationary states given by:

- $E_0 = (0, 0, 1, 0, 0)$ corresponding to the tumor-free equilibrium.
- If $t_0 < 1$, then $E_T = \left(1 - t_0, 0, \frac{\varrho_0}{\varrho_0 + \gamma_0(1 - t_0)}, \frac{1 - t_0}{\eta_0}, 0\right)$ corresponds to the bacteria-free tumor equilibrium.
- If the following conditions

$$\begin{aligned} t_0 &< 1; \\ b_0 &< \mu_0 \frac{\kappa}{1 + \kappa}; \\ b_0 + \frac{\beta_0}{\eta_0}(1 - t_0) &> \frac{\mu_0 \kappa (\varrho_0 + \gamma_0(1 - t_0))}{\kappa (\varrho_0 + \gamma_0(1 - t_0)) + \varrho_0}, \end{aligned} \quad (39)$$

are met,

then $E_* = \left(\bar{T}, \frac{\lambda_0}{\alpha_0}(1 - t_0 - \bar{T}), \frac{\varrho_0}{\varrho_0 + \gamma_0 \bar{T}}, \frac{\bar{T}}{\eta_0}, \frac{1}{\alpha_0}(1 - t_0 - \bar{T})\right)$ corresponds to the coexistence equilibrium, where $\bar{T} \in]0, 1 - t_0[$ satisfies the quadratic equation:

$$\mu_0 \frac{\kappa (\varrho_0 + \gamma_0 \bar{T})}{\kappa (\varrho_0 + \gamma_0 \bar{T}) + \varrho_0} = b_0 + \frac{\beta_0}{\eta_0} \bar{T}. \quad (40)$$

Proof 4. A spatially homogeneous steady state $(\bar{T}, \bar{B}, \bar{O}, \bar{I}, \bar{S})$ of (37) satisfies:

$$\begin{aligned} \partial_t T &= \partial_t B = \partial_t O = \partial_t I = \partial_t S = 0, \\ \Delta T &= \Delta B = \Delta O = \Delta I = \Delta S = 0. \end{aligned}$$

Thus, the steady states are solutions of the system

$$\begin{cases} 0 = \bar{T}(1 - \bar{T}) - t_0 \bar{T} - \alpha_0 \bar{S} \bar{T}, \\ 0 = \mu_0 \bar{B} \frac{\kappa}{\kappa + \bar{O}} - b_0 \bar{B} - \beta_0 \bar{I} \bar{B}, \\ 0 = -\gamma_0 \bar{T} \bar{O} + \varrho_0(1 - \bar{O}), \\ 0 = \bar{T} - \eta_0 \bar{I}, \\ 0 = \bar{B} - \lambda_0 \bar{S}. \end{cases} \quad (41)$$

From the last two equations we obtain

$$\bar{I} = \frac{\bar{T}}{\eta_0}, \quad \bar{S} = \frac{\bar{B}}{\lambda_0}. \quad (42)$$

Moreover, in the third equation of (41) the oxygen density satisfies

$$\bar{O} = \frac{\varrho_0}{\varrho_0 + \gamma_0 \bar{T}}. \quad (43)$$

Substituting (42) into the first two equations of (41) gives

$$0 = \bar{T} \left(1 - \bar{T} - t_0 - \alpha_0 \frac{\bar{B}}{\lambda_0}\right), \quad (44)$$

$$0 = \bar{B} \left(\mu_0 \frac{\kappa}{\kappa + \bar{O}} - b_0 - \beta_0 \frac{\bar{T}}{\eta_0}\right). \quad (45)$$

We now identify the possible steady states.

• **Tumor-free equilibrium.** If $\bar{T} = \bar{B} = 0$, then according to (42) $\bar{I} = 0$, $\bar{S} = 0$ and from (43) we obtain $\bar{O} = 1$. Thus the tumor-free equilibrium is

$$E_0 = (0, 0, 1, 0, 0).$$

• **Bacteria-free tumor equilibrium.** If $\bar{B} = 0$, then $\bar{S} = 0$ and (44)-(45) becomes

$$\bar{T}(1 - \bar{T} - t_0) = 0.$$

Hence $\bar{T} > 0$, if $t_0 < 1$ i.e., $\delta_T < \rho_T$, we obtain $\bar{T} = 1 - t_0$. From (42) and (43), the variables \bar{I}, \bar{O} are

$$\bar{I} = \frac{1 - t_0}{\eta_0}, \quad \bar{O} = \frac{\varrho_0}{\varrho_0 + \gamma_0(1 - t_0)}.$$

Therefore the tumor equilibrium without bacteria is

$$E_T = \left(1 - t_0, 0, \frac{\varrho_0}{\varrho_0 + \gamma_0(1 - t_0)}, \frac{1 - t_0}{\eta_0}, 0\right).$$

• **Coexistence equilibrium.** If $\bar{T} > 0$ and $\bar{B} > 0$, from (44), (42) and (43) we obtain

$$\bar{T} = 1 - t_0 - \alpha_0 \frac{\bar{B}}{\lambda_0}; \bar{I} = \frac{\bar{T}}{\eta_0}; \bar{S} = \frac{\bar{B}}{\lambda_0}; \bar{O} = \frac{\varrho_0}{\varrho_0 + \gamma_0 \bar{T}}. \quad (46)$$

Then, according to (45) the coexistence equilibrium satisfy the condition

$$\mu_0 \frac{\kappa}{\kappa + \bar{O}} = b_0 + \beta_0 \frac{\bar{T}}{\eta_0}. \quad (47)$$

We now determine the positive coexistence steady state $E_* = (\bar{T}, \bar{B}, \bar{O}, \bar{I}, \bar{S})$. For that, suppose that conditions (39) are met.

Substituting $\bar{O} = \varrho_0 / (\varrho_0 + \gamma_0 \bar{T})$ in equation (47) we have an quadratic equation for \bar{T} :

$$\mu_0 \frac{\kappa(\varrho_0 + \gamma_0 \bar{T})}{\kappa(\varrho_0 + \gamma_0 \bar{T}) + \varrho_0} = b_0 + \frac{\beta_0}{\eta_0} \bar{T}. \quad (48)$$

Let define the function f in \mathbb{R}_+ such that

$$f(\xi) = \mu_0 \frac{\kappa(\varrho_0 + \gamma_0 \xi)}{\kappa(\varrho_0 + \gamma_0 \xi) + \varrho_0} - b_0 - \frac{\beta_0}{\eta_0} \xi.$$

Equation (48) can be rewritten as

$$f(\bar{T}) = 0. \quad (49)$$

We have

$$\begin{aligned} f(0) &= \mu_0 \frac{\kappa}{1 + \kappa} - b_0, \\ f(1 - t_0) &= \mu_0 \frac{\kappa(\varrho_0 + \gamma_0(1 - t_0))}{\kappa(\varrho_0 + \gamma_0(1 - t_0)) + \varrho_0} \\ &\quad - b_0 - \frac{\beta_0}{\eta_0}(1 - t_0). \end{aligned} \quad (50)$$

According to conditions (39), we obtain $f(0) > 0$ and $f(1 - t_0) < 0$ and since f is continuous on \mathbb{R}_+ , then the

equation (49) has at least one solution \bar{T} in $]0, 1 - t_0[$. Once the existence of $\bar{T} \in]0, 1 - t_0[$ is established, then from (46) and according to (39) again we have

$$\begin{aligned} \bar{B} &= \frac{\lambda_0}{\alpha_0}(1 - t_0 - \bar{T}) > 0; \quad \bar{I} = \frac{\bar{T}}{\eta_0}; \\ \bar{S} &= \frac{1}{\alpha_0}(1 - t_0 - \bar{T}); \quad \bar{O} = \frac{\varrho_0}{\varrho_0 + \gamma_0 \bar{T}}. \end{aligned} \quad (51)$$

Therefore, we have the existence of the coexistence equilibrium $E_* = (\bar{T}, \bar{B}, \bar{O}, \bar{I}, \bar{S})$ where $\bar{T} \in]0, 1 - t_0[$ satisfies (48) and $\bar{B}, \bar{O}, \bar{I}, \bar{S}$ are given by (51), which terminates the proof of Proposition 3.2.

3.4. Stability analysis of the steady states

We analyze the stability of the homogeneous system derived from (37). This allows us to establish the conditions of the stability of equilibrium states, taking into account the formation of spatial patterns. Let $E = (\bar{T}, \bar{B}, \bar{O}, \bar{I}, \bar{S})$ be a homogeneous equilibrium described Proposition 3.2. We study the local stability of the homogeneous equilibrium states E . Let $\mathbf{U} = (T, B, O, I, S)^T$ solution of (37). The system (37) can be rewritten in the abstract form (17) with

$$\partial_t \mathbf{U} = \mathbf{D} \Delta \mathbf{U} + \mathbf{F}(\mathbf{U}),$$

where $\mathbf{D} = \text{diag}(1, d_B, d_O, d_I, d_S)$ and $\mathbf{F}(\mathbf{U})$ the reaction operator terms in (37).

Now, by linearize the system around E by writing $\mathbf{U} = E + u$, we have that the perturbation term u satisfies

$$\partial_t u = \mathbf{D} \Delta u + \mathbf{J}(E)u, \quad (52)$$

where $\mathbf{J}(E)$ is the Jacobian matrix of \mathbf{F} evaluated at E defined by

$$\mathbf{J}(E) = \begin{pmatrix} 1 - 2\bar{T} - t_0 - \alpha_0 \bar{S} & 0 & 0 & 0 & 0 & -\alpha_0 \bar{T} \\ 0 & \mu_0 \frac{\kappa}{\kappa + \bar{O}} - b_0 - \beta_0 \bar{I} & -\mu_0 \bar{B} \frac{\kappa}{(\kappa + \bar{O})^2} & -\beta_0 \bar{B} & 0 & 0 \\ -\gamma_0 \bar{O} & 0 & -\gamma_0 \bar{T} - \varrho_0 & 0 & 0 & 0 \\ 1 & 0 & 0 & 0 & -\eta_0 & 0 \\ 0 & 1 & 0 & 0 & 0 & -\lambda_0 \end{pmatrix}.$$

Due to Neumann's boundary conditions in (37), the following Laplacian eigenvalue problem

$$-\Delta \phi_k = \lambda_k \phi_k$$

admits a sequence of positive eigenvalues $(\lambda_k)_{k=1, \dots, 5}$ such that $\lambda_1 = 0 < \lambda_k$ for all $k = 2, \dots, 5$ which correspond respectively to scalar eigenfunctions $(\phi_k)_{k=1, \dots, 5}$.

We assume that the perturbation u as in the form

$$u(x, t) = \sum_k c_k(t) \phi_k(x),$$

where the function $c_k \in C^1([0, \tau]; \mathbb{R}^5)$, and substituting into the linearized equation (52) gives for all $k = 1, \dots, 5$:

$$\frac{dc_k}{dt} = (\mathbf{J}(E) - \lambda_k \mathbf{D}) c_k. \quad (53)$$

Therefore the stability of the equilibrium E is determined by the eigenvalues of the matrices M_k , $k = 1, \dots, 5$ such that:

$$M_k = \mathbf{J}(E) - \lambda_k \mathbf{D}. \quad (54)$$

We have the following results

Proposition 3.3. • The tumor-free equilibrium

$$E_0 = (0, 0, 1, 0, 0)$$

is locally asymptotically stable if

$$t_0 > 1 \quad \text{and} \quad \mu_0 \frac{\kappa}{\kappa + 1} < b_0. \quad (55)$$

• The tumor equilibrium

$$E_T = \left(1 - t_0, 0, \frac{\rho_0}{\rho_0 + \gamma_0(1 - t_0)}, \frac{1 - t_0}{\eta_0}, 0 \right)$$

exists for $t_0 < 1$ and is locally asymptotically stable if

$$\mu_0 \frac{\kappa}{\kappa + \bar{O}} < b_0 + \beta_0 \frac{1 - t_0}{\eta_0}, \quad (56)$$

$$\text{where } \bar{O} = \frac{\rho_0}{\rho_0 + \gamma_0(1 - t_0)}.$$

• The coexistence equilibrium

$$E_* = (\bar{T}, \bar{B}, \bar{O}, \bar{I}, \bar{S})$$

is locally asymptotically stable if there exists.

Proof 5. • The tumor-free equilibrium $E_0 = (0, 0, 1, 0, 0)$.

Assume that $t_0 > 1$, and $\mu_0 \frac{\kappa}{\kappa + 1} < b_0$. Evaluating M_k at E_0 $k = 1, \dots, 5$ gives

$$M_k(E_0) = \begin{pmatrix} 1 - t_0 - \lambda_k & 0 & 0 & 0 & 0 \\ 0 & \mu_0 \frac{\kappa}{\kappa + 1} - b_0 - \lambda_k d_B & 0 & 0 & 0 \\ -\gamma_0 & 0 & -\rho_0 - \lambda_k d_O & 0 & 0 \\ 1 & 0 & 0 & -\eta_0 - \lambda_k d_I & 0 \\ 0 & 1 & 0 & 0 & -\lambda_0 - \lambda_k d_S \end{pmatrix}$$

Since $\lambda_k \geq 0$ and coefficients $d_B, d_O, d_I, d_S \geq 0$, then all real eigenvalues of $M_k(E_0)$ are negative. Hence E_0 is locally asymptotically stable.

• Bacteria-free tumor equilibrium:

$E_T = (1 - t_0, 0, \frac{\rho_0}{\rho_0 + \gamma_0(1 - t_0)}, \frac{1 - t_0}{\eta_0}, 0)$. Assume that $t_0 < 1$ and the condition (56) is satisfied. For $k = 1, \dots, 5$ the eigenvalues of $M_k(E_T)$ are given by

$$\begin{aligned} \xi_1 &= -(1 - t_0) - \lambda_k \leq 0, \\ \xi_2 &= \mu_0 \frac{\kappa}{\kappa + \bar{O}} - b_0 - \beta_0 \bar{I} - \lambda_k d_B \leq 0, \\ \xi_3 &= -\gamma_0(1 - t_0) - \rho_0 - \lambda_k d_O \leq 0, \\ \xi_4 &= -\eta_0 - \lambda_k d_I \leq 0, \\ \xi_5 &= -\lambda_0 - \lambda_k d_S \leq 0. \end{aligned}$$

Then, all real eigenvalues of $M_k(E_T)$ are negative. Therefore E_T is locally asymptotically stable under the condition (56).

• The coexistence equilibrium $E_* = (\bar{T}, \bar{B}, \bar{O}, \bar{I}, \bar{S})$ satisfying (51) and (48). After calculating all nonzero coefficients of $J(E_*)$, the matrix $M_k(E_*)$ is:

$$M_k(E_*) = \begin{pmatrix} -\bar{T} - \lambda_k & 0 & 0 & 0 & -\alpha_0 \bar{T} \\ 0 & -\lambda_k d_B & -\mu_0 \bar{B} \frac{\kappa}{(\kappa + \bar{O})^2} & -\beta_0 \bar{B} & 0 \\ -\gamma_0 \bar{O} & 0 & -\gamma_0 \bar{T} - \rho_0 - \lambda_k d_O & 0 & 0 \\ 1 & 0 & 0 & -\eta_0 - \lambda_k d_I & 0 \\ 0 & 1 & 0 & 0 & -\lambda_0 - \lambda_k d_S \end{pmatrix}.$$

The eigenvalues of the matrix $M_k(E_*)$ are given by

$$\begin{aligned} \xi_1 &= -\bar{T} - \lambda_k \leq 0, \\ \xi_2 &= -\eta_0 - \lambda_k d_I \leq 0, \\ \xi_3 &= -\lambda_0 - \lambda_k d_S \leq 0, \\ \xi_4 &= -\gamma_0 \bar{T} - \rho_0 - \lambda_k d_O \leq 0, \\ \xi_5 &= -\lambda_k d_B \leq 0. \end{aligned} \quad (57)$$

Then, all spatial perturbations decay exponentially and the coexistence equilibrium E_* is locally asymptotically stable. For $k = 0$, we have $\xi_5 = 0$, and thus E_* is non-hyperbolic for the homogeneous system in space, but remains stable with respect to spatial perturbations.

Remark 3.2. The diffusion introduces the terms $-\lambda_k \mathbf{D}$, which shift the eigenvalues toward the negative half-plane. Then, for $k > 0$, no eigenvalues of $M_k(E_*)$ become positive, and diffusion cannot destabilize the equilibrium. Therefore, no Turing instability is induced by diffusion [35].

4. PINNs Approximation

Solving system (8) numerically poses specific challenges that motivate the use of PINNs. Classical mesh-based methods such as finite elements or finite differences require a spatial mesh whose resolution must be adapted to the three orders-of-magnitude gap between the fastest diffusion coefficient, and must handle the stiff vascular exchange term through costly implicit time-stepping. Beyond these technical difficulties, the five nonlinearly coupled equations require either operator-splitting which introduces splitting errors or the assembly of large block Jacobians at each Newton step.

PINNs [41] circumvent all three issues simultaneously: spatial and temporal coordinates are treated as continuous inputs, derivatives are computed exactly by automatic differentiation with no truncation error, and all five equations are enforced simultaneously as soft constraints on a single trainable loss, with no mesh and no time-stepping stability condition to satisfy. The mathematical analysis of Section 3.1 guarantees the existence and uniqueness of a solution $\mathbf{U} = (T, B, O, I, S)^T \in (C([0, \tau]; L^2(\Omega)) \cap L^2(0, \tau; H^1(\Omega)))^5$ to system (8). To compute this solution numerically, we employ a PINNs [41, 13, 12], an approach that embeds the governing equations, initial conditions, and boundary conditions directly into the loss functional of a deep neural network, thereby transforming the PDE problem into an unconstrained optimisation problem over the network weights. In this context recently many paper have focused on the using the deep learning methods for solving the he

The fundamental idea is to seek an approximation

$$\hat{\mathbf{U}}_\theta : \mathcal{Q} \longrightarrow \mathbb{R}^5, \quad (58)$$

realised by a single feedforward network $\mathcal{N}_\theta : \mathbb{R}^3 \rightarrow \mathbb{R}^5$ with trainable parameters θ , such that $\hat{\mathbf{U}}_\theta \approx \mathbf{U}$ in the sense

of minimising a physics-based loss defined below. Because no labelled simulation data are required, the method is *fully unsupervised*: the only supervision comes from the physical laws encoded in (8).

4.1. Network Architecture

The neural network \mathcal{N}_θ maps the spatio-temporal coordinate $(x, y, t) \in \Omega \times (0, \tau)$ to the five-dimensional state vector:

$$\mathcal{N}_\theta(x, y, t) = (\hat{T}, \hat{B}, \hat{O}, \hat{I}, \hat{S})(x, y, t). \quad (59)$$

We employ a fully connected Multi-Layer Perceptron (MLP) architecture consisting of L layers. The architecture comprises an input layer, several hidden layers of uniform width, and an output layer corresponding to the state variables. The hidden-layer activation is the hyperbolic tangent $\sigma(z) = \tanh(z)$. This choice is motivated by its infinite differentiability, which ensures that the high-order partial derivatives required for the differential operators in system (8) can be computed accurately through automatic differentiation without interpolation errors. Let $\mathbf{h}^{(0)} = (x, y, t)^\top$; the forward pass reads

$$\mathbf{h}^{(\ell)} = \sigma(\mathbf{W}^{(\ell)}\mathbf{h}^{(\ell-1)} + \mathbf{b}^{(\ell)}), \quad \ell = 1, \dots, L-1, \quad (60)$$

$$\mathcal{N}_\theta(x, y, t) = \mathbf{W}^{(L)}\mathbf{h}^{(L-1)} + \mathbf{b}^{(L)}, \quad (61)$$

where $\{\mathbf{W}^{(\ell)}, \mathbf{b}^{(\ell)}\}_{\ell=1}^L$ are the weight matrices and bias vectors collected in θ . Weights are initialised using the Xavier uniform scheme, which keeps the variance of activations stable across layers and accelerates convergence [16].

4.2. Derivative Computation via Automatic Differentiation

For every scalar network output $\hat{\varphi} \in \{\hat{T}, \hat{B}, \hat{O}, \hat{I}, \hat{S}\}$, all partial derivatives required by the residual operators of (8) are computed exactly by reverse-mode automatic differentiation (AD) [38], implemented in PyTorch. Concretely:

- **First-order derivatives** $\partial_x \hat{\varphi}, \partial_y \hat{\varphi}, \partial_t \hat{\varphi}$: one backward pass through the computation graph.
- **Laplacian** $\Delta \hat{\varphi} = \partial_{xx} \hat{\varphi} + \partial_{yy} \hat{\varphi}$: a second backward pass applied to $\partial_x \hat{\varphi}$ and $\partial_y \hat{\varphi}$, respectively.

This avoids any finite-difference truncation error and removes the mesh dependency from derivative computation entirely.

4.3. Collocation Point Sampling

Three disjoint sets of collocation points are drawn to enforce system (8):

Interior (PDE) points S_{pde} : A set of N_{pde} collocation points $(x_k, y_k, t_k) \in \mathcal{Q}$ sampled uniformly, with $(x_k, y_k) \sim \mathbf{U}(\Omega)$ and $t_k \sim \mathbf{U}(0, \tau)$.

Initial condition points S_{ic} : A set of N_{ic} points $(x_k, y_k, 0) \in \Omega \times \{0\}$ drawn uniformly over Ω .

Boundary points S_{bc} : A set of N_{bc} points $(x_k, y_k, t_k) \in \partial\Omega \times (0, \tau)$, drawn uniformly on each of the four sides of $\partial\Omega$, with $t_k \sim \mathbf{U}(0, \tau)$.

In practice the union $\mathcal{S} = S_{\text{pde}} \cup S_{\text{ic}} \cup S_{\text{bc}}$ is partitioned into training (60%), validation (20%), and test (20%) subsets.

4.4. Composite Loss Functional

The total loss to be minimised over θ is

$$\mathcal{L}(\theta) = \lambda_{\text{pde}} \mathcal{L}_{\text{pde}}(\theta) + \lambda_{\text{ic}} \mathcal{L}_{\text{ic}}(\theta) + \lambda_{\text{bc}} \mathcal{L}_{\text{bc}}(\theta), \quad (62)$$

where the weights are set to $\lambda_{\text{pde}}, \lambda_{\text{ic}}, \lambda_{\text{bc}}$. These weights play an important role in the convergence of the PINNs loss. In particular, choosing $\lambda_{\text{ic}} > \lambda_{\text{pde}}$ ensures that the network remains consistent with the prescribed initial conditions (see (6)). This weighting ensures that the learned spatio-temporal solution follows the given initial profiles. If the initial-condition term is assigned too little weight, the model may focus on reducing the PDE residual, which can cause it to converge to the trivial solution $\mathbf{U} \equiv 0$ instead of the intended physical solution.

1. **PDE Residual Loss:** The five residual operators $\mathcal{R}_T, \mathcal{R}_B, \mathcal{R}_O, \mathcal{R}_I, \mathcal{R}_S$ are obtained by substituting the network outputs into the left-hand sides of (8):

$$\begin{aligned} \mathcal{R}_T &= \partial_t \hat{T} - D_T \Delta \hat{T} - \rho_T \hat{T} \left(1 - \frac{\hat{T}}{c}\right) \\ &\quad + \delta_T \hat{T} + \alpha_S \hat{S} \hat{T}; \end{aligned} \quad (63a)$$

$$\begin{aligned} \mathcal{R}_B &= \partial_t \hat{B} - D_B \Delta \hat{B} - \rho_B \hat{B} \frac{K_H}{K_H + \hat{O}} \\ &\quad + \delta_B \hat{B} + \beta_I \hat{I} \hat{B}; \end{aligned} \quad (63b)$$

$$\begin{aligned} \mathcal{R}_O &= \partial_t \hat{O} - D_O \Delta \hat{O} + \gamma_T \hat{T} \hat{O} \\ &\quad - \gamma_{\text{vas}} (O_{\text{vas}} - \hat{O}); \end{aligned} \quad (63c)$$

$$\mathcal{R}_I = \partial_t \hat{I} - D_I \Delta \hat{I} - \beta_T \hat{T} + \delta_I \hat{I}; \quad (63d)$$

$$\mathcal{R}_S = \partial_t \hat{S} - D_S \Delta \hat{S} - \beta_B^{(S)} \hat{B} + \delta_S \hat{S}. \quad (63e)$$

Setting $\mathcal{V} := \{T, B, O, I, S\}$, the PDE loss is then the mean-squared residual over S_{pde} :

$$\mathcal{L}_{\text{pde}}(\theta) = \frac{1}{N_{\text{pde}}} \sum_{k=1}^{N_{\text{pde}}} \sum_{\varphi \in \mathcal{V}} [\mathcal{R}_\varphi(x_k, y_k, t_k; \theta)]^2. \quad (64)$$

2. **Initial Condition Loss:** The initial condition loss enforces (6) at $t = 0$:

$$\mathcal{L}_{\text{ic}}(\theta) = \frac{1}{N_{\text{ic}}} \sum_{k=1}^{N_{\text{ic}}} \sum_{\varphi \in \mathcal{V}} [\hat{\varphi}(x_k, y_k, 0; \theta) - \varphi_0(x_k, y_k)]^2, \quad (65)$$

where φ_0 denotes the initial profile of each species given in (6). Concretely, we consider the following initial conditions:

$$T_0(x, y) = \exp\left(-\frac{\|(x, y) - \mathbf{x}_T\|^2}{2\sigma_T^2}\right), \quad (66a)$$

$$B_0(x, y) = 0.3 \exp\left(-\frac{\|(x, y) - \mathbf{x}_B\|^2}{2\sigma_B^2}\right), \quad (66b)$$

$$O_0(x, y) = O_{\text{vas}}, \quad I_0(x, y) = 0.01, \\ S_0(x, y) = 0, \quad (66c)$$

where, the tumor centre is $\mathbf{x}_T = (L/2, L/2)$, $\mathbf{x}_B = (0.3L, 0.6L)$ is the bacterial injection site, $\sigma_T = L/5$ and $\sigma_B = L/8$ are the spatial spreads, and $L = 6$ mm. The Gaussian profile (66a) initialises a localised tumour seed at 10% of the carrying capacity θ , while (66b) places a very small bacterial inoculum ($B_0 \ll T_0$) at an off-centre position, simulating a targeted injection away from the tumour core.

3. Boundary Condition Loss

The homogeneous Neumann conditions (7) are enforced by penalising the squared gradient norm on S_{bc} :

$$\mathcal{L}_{\text{bc}}(\theta) = \frac{1}{N_{\text{bc}}} \sum_{k=1}^{N_{\text{bc}}} \sum_{\varphi \in \mathcal{V}} \left\| \nabla_{(x,y)} \hat{\varphi}(x_k, y_k, t_k; \theta) \right\|^2. \quad (67)$$

Note that the gradient $\nabla_{(x,y)} \hat{\varphi}$ is again computed exactly via AD, so no approximation of the outward normal \mathbf{n} is needed.

Proposition 4.1 (Consistency of the PINN loss). *Let θ^* be such that $\mathcal{L}(\theta^*) = 0$. Then the network \mathcal{N}_{θ^*} satisfies the residuals $\mathcal{R}_\varphi \equiv 0$ for all φ at every collocation point in S_{pde} , reproduces the initial data at every point in S_{ic} , and satisfies the zero-flux condition at every point in S_{bc} .*

More details about the numerical parameters and implementation details are described in the section 6.

In the next section, we provide a rigorous convergence analysis of the proposed PINN framework and establish error estimates for the method.

5. Convergence Analysis of the PINN Approximation

Let $\mathbf{U} = (T, B, O, I, S)^\top$ be the unique classical solution of system (8) corresponding to the initial data \mathbf{U}_0 (guaranteed by Theorem 3.1-Proposition 3.1), and let $\hat{\mathbf{U}}_\theta = (\hat{T}, \hat{B}, \hat{O}, \hat{I}, \hat{S})^\top$ be the PINN approximation produced by the network $\mathcal{N}_\theta : \mathbb{R}^3 \rightarrow \mathbb{R}^5$ after minimizing the composite loss (62). Define the *total approximation error* as

$$\mathbf{e}(t, \mathbf{x}) = \mathbf{U}(t, \mathbf{x}) - \hat{\mathbf{U}}_\theta(t, \mathbf{x}), \quad (t, \mathbf{x}) \in \mathcal{Q}. \quad (68)$$

The total error admits the three-way decomposition:

$$\|\mathbf{e}\|_{L^\infty(0,\tau;(L^2(\Omega))^5)} \leq \underbrace{\mathcal{E}_{\text{approx}}(\theta)}_{\text{(I) approximation}} + \underbrace{\mathcal{E}_{\text{gen}}(N)}_{\text{(II) generalization}} \\ + \underbrace{\mathcal{E}_{\text{opt}}(\theta^*)}_{\text{(III) optimisation}}, \quad (69)$$

where:

Algorithm 1 PINN Training for System (8)

Require: Collocation sets $S_{\text{pde}}, S_{\text{ic}}, S_{\text{bc}}$; weights $\lambda_{\text{pde}}, \lambda_{\text{ic}}, \lambda_{\text{bc}}$; A patience P ; the maximum epochs E .

Ensure: Best-validation-loss weights θ^* .

- 1: Initialise θ with Xavier uniform distribution.
 - 2: $\mathcal{L}^* \leftarrow +\infty$; $p \leftarrow 0$.
 - 3: **for** $e = 1, \dots, E$ **do**
 - 4: Sample mini-batch of size 512 from each collocation set.
 - 5: Compute $\mathcal{L}(\theta)$ via forward pass + AD (Sec. 4.2).
 - 6: Update $\theta \leftarrow \theta - \eta \nabla_\theta \mathcal{L}(\theta)$ via Adam.
 - 7: Evaluate \mathcal{L}_{val} on the held-out validation set.
 - 8: **if** $\mathcal{L}_{\text{val}} < \mathcal{L}^*$ **then**
 - 9: $\mathcal{L}^* \leftarrow \mathcal{L}_{\text{val}}$; $\theta^* \leftarrow \theta$; $p \leftarrow 0$.
 - 10: **else**
 - 11: $p \leftarrow p + 1$.
 - 12: **end if**
 - 13: **if** $p \geq P$ **then break** ▷ Early stopping
 - 14: **end if**
 - 15: Adjust η via ReduceLRonPlateau scheduler.
 - 16: **end for**
 - 17: **return** θ^* .
-

- (I) **Approximation error:** the best-achievable error of a depth- L , width- n network in approximating the true solution $\mathbf{U} \in (L^2(0, \tau; H^1(\Omega)))^5$.
- (II) **Generalization error:** the discrepancy between the empirical (Monte Carlo) loss evaluated on $N_{\text{pde}}, N_{\text{ic}}, N_{\text{bc}}$ collocation points and the continuous L^2 -residuals over \mathcal{Q}, Ω , and Σ .
- (III) **Optimisation error:** the gap between the loss achieved by the Adam algorithm after E epochs and the global minimum of the loss landscape.

Item (III) depends on the specific optimization trajectory and is not addressed here; we provide upper bounds for (I) and (II), and we derive a conditional stability estimate showing that if (I) and (II) are small, then $\|\mathbf{e}\|_{L^\infty(0,\tau;(L^2(\Omega))^5)}$ is small.

We begin by defining the continuous residual functionals associated with the PINN approximation \mathbf{U}_θ .

5.1. Continuous Residual Functionals

Define the *continuous* (true) residuals associated with the PINN approximation $\hat{\mathbf{U}}_\theta$:

$$\mathcal{E}_{\text{pde}}(\theta) = \int_0^\tau \int_\Omega \sum_{\varphi \in \mathcal{V}} \left| \mathcal{R}_\varphi(\hat{\mathbf{U}}_\theta; t, \mathbf{x}) \right|^2 \mathrm{d}\mathbf{x} \mathrm{d}t, \quad (70)$$

$$\mathcal{E}_{\text{ic}}(\theta) = \int_\Omega \sum_{\varphi \in \mathcal{V}} \left| \hat{\varphi}(\mathbf{x}, 0; \theta) - \varphi_0(\mathbf{x}) \right|^2 \mathrm{d}\mathbf{x}, \quad (71)$$

$$\mathcal{E}_{\text{bc}}(\theta) = \int_0^\tau \int_{\partial\Omega} \sum_{\varphi \in \mathcal{V}} \left| \nabla_{\mathbf{x}} \hat{\varphi}(\mathbf{x}, t; \theta) \cdot \mathbf{n} \right|^2 \mathrm{d}\sigma \mathrm{d}t, \quad (72)$$

Table 1

The numerical simulation parameters of the system (8)

Equation	Description	Symbol	Value	Unit
All	Tumor cell motility	D_T	0.01	$\text{mm}^2 \text{day}^{-1}$
	Bacterial diffusivity	D_B	0.1	$\text{mm}^2 \text{day}^{-1}$
	Oxygen diffusivity	D_O	1.0	$\text{mm}^2 \text{day}^{-1}$
	Cytokine diffusivity	D_I	0.5	$\text{mm}^2 \text{day}^{-1}$
	AHL signal diffusivity	D_S	0.3	$\text{mm}^2 \text{day}^{-1}$
(1) Tumor T	Proliferation rate	ρ_T	0.3	day^{-1}
	Carrying capacity	θ	1.0	normalised
	Apoptosis rate	δ_T	0.05	day^{-1}
	Signal suppression coeff.	α_S	0.2	day^{-1}
(2) Bacteria B	Growth/clearance rate	ρ_B	0.5	day^{-1}
	O ₂ half-saturation	K_H	0.1	normalised
	Natural death rate	δ_B	0.1	day^{-1}
	Immune clearance efficiency	β_I	0.3	day^{-1}
(3) Oxygen O	Tumor O ₂ consumption	γ_T	0.2	day^{-1}
	Vascular exchange rate	γ_E	0.5	day^{-1}
	Baseline O ₂ level	O_{ext}	0.2	normalised
(4) Cytokines I	Tumor-derived production	β_T	0.1	day^{-1}
	Cytokine decay rate	δ_I	0.2	day^{-1}
(5) Signal S	production rate	β_B	0.4	day^{-1}
	degradation rate	δ_S	0.3	day^{-1}

where \mathcal{R}_φ are the five residual operators defined in (63). Let $\mathcal{E}(\theta) = \lambda_{\text{pde}} \mathcal{E}_{\text{pde}} + \lambda_{\text{ic}} \mathcal{E}_{\text{ic}} + \lambda_{\text{bc}} \mathcal{E}_{\text{bc}}$ denote the total continuous loss.

5.2. Lipschitz Continuity of the Nonlinear Operator

In this section, we first establish that the nonlinear function $F : \mathbb{R}^5 \rightarrow \mathbb{R}^5$ defined in (11) is locally Lipschitz.

Lemma 5.1 (Lipschitz bound on F). *There exists a constant $L_F > 0$ such that*

$$\|F(\mathbf{U}) - F(\hat{\mathbf{U}}_\theta)\|_{(L^2(\Omega))^5} \leq L_F \|\mathbf{e}\|_{(L^2(\Omega))^5}, \quad \text{a.e. } t \in (0, \tau). \quad (73)$$

Proof 6. *Theorem 3.1 guarantees $\mathbf{U} \in (L^\infty(Q)_+)^5$ whenever $\mathbf{U}_0 \in (H^1(\Omega) \cap (L^\infty(\Omega)_+)^5$. For the network approximation $\hat{\mathbf{U}}_\theta$, boundedness is enforced by the bounded weight initialisation and the tanh activation (whose output is always in $(-1, 1)$). Then, there exists constants M such that $\|\mathbf{U}\|_{(L^\infty(Q))^5} \leq M$, and $\|\hat{\mathbf{U}}_\theta\|_{(L^\infty(Q))^5} \leq M$. Now, recall*

from (11) the five components of F :

$$F_T(\mathbf{U}) = \rho_T T \left(1 - \frac{T}{c}\right) - \delta_T T - \alpha_S S T;$$

$$F_B(\mathbf{U}) = \rho_B B \frac{K_H}{K_H + O} - \delta_B B - \beta_I I B;$$

$$F_O(\mathbf{U}) = -\gamma_T T O + \gamma_{\text{vas}} (O_{\text{vas}} - O);$$

$$F_I(\mathbf{U}) = \beta_T T - \delta_I I;$$

$$F_S(\mathbf{U}) = \beta_B B - \delta_S S.$$

We bound $F_\varphi(\mathbf{U}) - F_\varphi(\hat{\mathbf{U}}_\theta)$ in $L^2(\Omega)$ with $\varphi = T, B, O, I, S$. Let $e_\varphi = \varphi - \hat{\varphi}$ for each component.

Term F_T :

$$F_T(\mathbf{U}) - F_T(\hat{\mathbf{U}}_\theta) = (\rho_T - \delta_T) e_T - \frac{\rho_T}{c} (T + \hat{T}) e_T - \alpha_S (S T - \hat{S} \hat{T}).$$

Since $|T| \leq M$, $|\hat{T}| \leq M$ and using the assumption (H), the first term is bounded by $C_M \|e_T\|_{L^2(\Omega)}$. For the second term, using the fact that $S T - \hat{S} \hat{T} = S e_T + \hat{T} e_S$, and $|S| \leq M$, $|\hat{T}| \leq M$:

$$\|S T - \hat{S} \hat{T}\|_{L^2(\Omega)} \leq C_M \|e_T\|_{L^2(\Omega)} + C_M \|e_S\|_{L^2(\Omega)}.$$

Hence

$$\|F_T(\mathbf{U}) - F_T(\hat{\mathbf{U}}_\theta)\|_{L^2(\Omega)} \leq C_M (\|e_T\|_{L^2(\Omega)} + \|e_S\|_{L^2(\Omega)}). \quad (74)$$

Term F_B : For the fractional term, we have

$$B \frac{K_H}{K_H + O} - \hat{B} \frac{K_H}{K_H + \hat{O}} = \frac{(K_H^2 + K_H)\hat{O}e_B - K_H\hat{B}e_O}{(K_H + O)(K_H + \hat{O})}.$$

Since $O, \hat{O} \geq 0$, we have $(K_H + O)(K_H + \hat{O}) \geq K_H^2$, and using $|\hat{B}| \leq M$, $|\hat{O}| \leq M$ and assumption (H), we obtain:

$$\left\| B \frac{K_H}{K_H + O} - \hat{B} \frac{\hat{B}}{K_H + \hat{O}} \right\|_{L^2(\Omega)} \leq C_M (\|e_B\|_{L^2(\Omega)} + \|e_O\|_{L^2(\Omega)}).$$

For the rest of terms, we have

$$-\delta_B B + \delta_B \hat{B} - \beta_I I B + \beta_I \hat{I} \hat{B} = -\delta_B e_B - \beta_I (I e_B + \hat{B} e_I).$$

Using $|\hat{I}| \leq M$, $|\hat{B}| \leq M$ and assumption (H), we obtain:

$$\|F_B(\mathbf{U}) - F_B(\hat{\mathbf{U}}_\theta)\|_{L^2(\Omega)} \leq C_M (\|e_B\|_{L^2(\Omega)} + \|e_O\|_{L^2(\Omega)} + \|e_I\|_{L^2(\Omega)}). \quad (75)$$

Terms F_O, F_I, F_S : Using $|T|, |B|, |O| \leq M$, we have similarly obtained as the previous estimates, the following:

$$\|F_O(\mathbf{U}) - F_O(\hat{\mathbf{U}}_\theta)\|_{L^2(\Omega)} \leq C_M (\|e_T\|_{L^2(\Omega)} + \|e_B\|_{L^2(\Omega)} + \|e_O\|_{L^2(\Omega)}); \quad (76)$$

$$\|F_I(\mathbf{U}) - F_I(\hat{\mathbf{U}}_\theta)\|_{L^2(\Omega)} \leq C_M (\|e_T\|_{L^2(\Omega)} + \|e_I\|_{L^2(\Omega)}); \quad (77)$$

$$\|F_S(\mathbf{U}) - F_S(\hat{\mathbf{U}}_\theta)\|_{L^2(\Omega)} \leq C_M (\|e_B\|_{L^2(\Omega)} + \|e_S\|_{L^2(\Omega)}). \quad (78)$$

Summing estimates (74)-(78) with $\mathbf{e} = (e_T, e_B, e_O, e_I, e_S)^\top$, and setting $L_F = C_M$, completes the proof of Lemma 5.1.

5.2.1. Conditional Stability: Error Controlled by Residuals

The central result of this section shows that small PDE, IC, and BC residuals imply a small approximation error.

Theorem 5.1 (Conditional Stability). Let the assumptions of Theorem 3.1 hold and let $\hat{\mathbf{U}}_\theta \in (L^2(0, \tau; H^1(\Omega)) \cap H^1(0, \tau; (H^1(\Omega))'))^5$ be any network approximation. Define the total residual $\mathcal{E}(\theta) = \mathcal{E}_{\text{pde}}(\theta) + \mathcal{E}_{\text{ic}}(\theta) + \mathcal{E}_{\text{bc}}(\theta)$. Then there exists a constant $C = C(\tau, M, L_F, d_0) > 0$, independent of θ , such that

$$\sup_{t \in [0, \tau]} \|\mathbf{e}(t)\|_{(L^2(\Omega))^5}^2 + d_0 \int_0^\tau \|\nabla \mathbf{e}(s)\|_{(L^2(\Omega))^5}^2 ds \leq C \mathcal{E}(\theta). \quad (79)$$

Proof 7. Step 1 — Error equation. Since \mathbf{U} satisfies (10) exactly and $\hat{\mathbf{U}}_\theta$ satisfies it with residual $\mathbf{R}_\theta = (\mathcal{R}_T, \mathcal{R}_B, \mathcal{R}_O, \mathcal{R}_I, \mathcal{R}_S)^\top$, subtracting gives for a.e. $t \in (0, \tau)$:

$$\partial_t \mathbf{e} + \mathbf{A} \mathbf{e} = \mathbf{F}(\mathbf{U}) - \mathbf{F}(\hat{\mathbf{U}}_\theta) - \mathbf{R}_\theta \quad \text{in } \mathcal{Q}, \quad (80a)$$

$$\partial_n \mathbf{e} = -\partial_n \hat{\mathbf{U}}_\theta \quad \text{on } \Sigma, \quad (80b)$$

$$\mathbf{e}(0, \cdot) = \mathbf{U}_0 - \hat{\mathbf{U}}_\theta(\cdot, 0) \quad \text{in } \Omega. \quad (80c)$$

Step 2 — Energy identity. Take the $(L^2(\Omega))^5$ inner product of (80a) with \mathbf{e} and integrate over Ω . Integration by parts, using the boundary condition (80b), yields

$$\begin{aligned} & \frac{1}{2} \frac{d}{dt} \|\mathbf{e}(t)\|_{(L^2(\Omega))^5}^2 + (\mathbf{D} \nabla \mathbf{e}, \nabla \mathbf{e})_{(L^2(\Omega))^5} \\ &= (\mathbf{F}(\mathbf{U}) - \mathbf{F}(\hat{\mathbf{U}}_\theta), \mathbf{e})_{(L^2(\Omega))^5} - (\mathbf{R}_\theta, \mathbf{e})_{(L^2(\Omega))^5} \\ &+ \int_{\partial \Omega} \mathbf{D} \partial_n \hat{\mathbf{U}}_\theta \cdot \mathbf{e} \, d\sigma. \end{aligned} \quad (81)$$

Step 3 — Bounding the right-hand side of (81).

Nonlinear term. By Lemma 5.1:

$$(\mathbf{F}(\mathbf{U}) - \mathbf{F}(\hat{\mathbf{U}}_\theta), \mathbf{e})_{(L^2(\Omega))^5} \leq L_F \|\mathbf{e}\|_{(L^2(\Omega))^5}^2. \quad (82)$$

Residual term. By Young's inequality for all $\varepsilon > 0$:

$$\left| (\mathbf{R}_\theta, \mathbf{e})_{(L^2(\Omega))^5} \right| \leq \frac{1}{2\varepsilon} \|\mathbf{R}_\theta\|_{(L^2(\Omega))^5}^2 + \frac{\varepsilon}{2} \|\mathbf{e}\|_{(L^2(\Omega))^5}^2. \quad (83)$$

Boundary term. Using the trace inequality in $L^2(\partial \Omega)$ (see [6, Theorem 1.6.6.]), and Young's inequality, we have for all $\varepsilon > 0$:

$$\begin{aligned} \left| \int_{\partial \Omega} \mathbf{D} \partial_n \hat{\mathbf{U}}_\theta \cdot \mathbf{e} \, d\sigma \right| &\leq \|\mathbf{D}\|_\infty \|\partial_n \hat{\mathbf{U}}_\theta\|_{(L^2(\partial \Omega))^5} \|\mathbf{e}\|_{(L^2(\partial \Omega))^5} \\ &\leq \frac{C_{d,\Omega}}{2\varepsilon} \|\partial_n \hat{\mathbf{U}}_\theta\|_{(L^2(\partial \Omega))^5}^2 \\ &+ \frac{\varepsilon C_{d,\Omega}}{2} (\varepsilon \|\nabla \mathbf{e}\|_{(L^2(\Omega))^5}^2 + \varepsilon^{-1} \|\mathbf{e}\|_{(L^2(\Omega))^5}^2). \end{aligned} \quad (84)$$

Step 4 — Differential inequality. Since from (17), $\mathbf{A} = -\mathbf{D} \mathbf{A}$ with $\mathbf{D} = \text{diag}(D_T, D_B, D_O, D_I, D_S)$, we have $(\mathbf{D} \nabla \mathbf{e}, \nabla \mathbf{e})_{(L^2(\Omega))^5} \geq d_0 \|\nabla \mathbf{e}\|_{(L^2(\Omega))^5}^2$, where $d_0 = \min(D_T, D_B, D_O, D_I, D_S)$. Substituting bounds (82)–(84) into (81), and choosing $\varepsilon = \sqrt{d_0/2C_{d,\Omega}}$ to absorb the gradient term:

$$\begin{aligned} \frac{d}{dt} \|\mathbf{e}\|_{(L^2(\Omega))^5}^2 + d_0 \|\nabla \mathbf{e}\|_{(L^2(\Omega))^5}^2 &\leq \Lambda \|\mathbf{e}\|_{(L^2(\Omega))^5}^2 \\ &+ C_1 \|\mathbf{R}_\theta\|_{(L^2(\Omega))^5}^2 \\ &+ C_2 \|\partial_n \hat{\mathbf{U}}_\theta\|_{(L^2(\partial \Omega))^5}^2, \end{aligned} \quad (85)$$

where $\Lambda = 2L_F + \varepsilon + C_{d,\Omega}$, $C_1 = \varepsilon^{-1}$, $C_2 = \varepsilon^{-1} C_{d,\Omega}$ are constants depending only on M , d_0 , and the trace constant $C_{d,\Omega}$.

Step 5 — Application of Grönwall's Lemma. Integrating (85) over $[0, t]$ and applying Grönwall's Lemma:

$$\|\mathbf{e}(t)\|_{(L^2(\Omega))^5}^2 + d_0 \int_0^t \|\nabla \mathbf{e}\|_{(L^2(\Omega))^5}^2 ds$$

$$\begin{aligned} &\leq e^{\Lambda\tau} \left[\|\mathbf{e}(0)\|_{(L^2(\Omega))^5}^2 \right. \\ &+ C_1 \int_0^\tau \int_\Omega \sum_{\varphi \in \mathcal{V}} |\mathcal{R}_\varphi|^2 d\mathbf{x} ds \\ &\left. + C_2 \int_0^\tau \int_{\partial\Omega} \sum_{\varphi \in \mathcal{V}} |\partial_{\mathbf{n}} \hat{\varphi}|^2 d\sigma ds \right]. \quad (86) \end{aligned}$$

Recognising

$$\begin{aligned} \|\mathbf{e}(0)\|_{(L^2)^5}^2 &= \mathcal{E}_{\text{ic}}(\theta); \quad \int_Q \sum |\mathcal{R}_\varphi|^2 = \mathcal{E}_{\text{pde}}(\theta); \\ \int_\Sigma \sum |\partial_{\mathbf{n}} \hat{\varphi}|^2 &= \mathcal{E}_{\text{bc}}(\theta), \end{aligned}$$

and taking the supremum over $t \in [0, \tau]$ gives (79) with $C = e^{\Lambda\tau} \max(1, C_1/\lambda_{\text{ic}}, C_2/\lambda_{\text{bc}}, C_1/\lambda_{\text{pde}})$.

Remark 5.1 (Role of the IC weight λ_{ic}). Estimate (79) shows that the error bound is proportional to $\mathcal{E}(\theta)$, which includes $\lambda_{\text{ic}} \mathcal{E}_{\text{ic}}$. A large λ_{ic} forces the optimiser to reduce \mathcal{E}_{ic} aggressively, thereby tightening the bound. This provides justification for the choice a higher λ_{ic} used in training.

5.2.2. Neural Network Approximation Capacity

We now address the question of a neural network's ability to approximate the exact solution of the pair system. The Proposition 3.1 gives the Sobolev regularities of the solution \mathbf{U} of the system (8) corresponding to the initial data $\mathbf{U}_0 \in (L^\infty(\Omega)_+ \cap H^1(\Omega))^5$. Precisely, we have $\mathbf{U} \in (L^2(0, \tau; H^2(\Omega)) \cap H^1(0, \tau; L^2(\Omega)))^5 =: (H^{2,1}(Q))^5$. Based on well-known classical results in the analysis of parabolic equations, this is natural Sobolev regularity of solutions to second-order parabolic systems with initial data $H^1(\Omega)$.

The regularity $H^{2,1}(Q)$ of the global solution of (8) is sufficient for estimating conditional stability (Theorem 5.1). However, the approximation theorem (Theorem 5.2) requires additional regularity of the global solution (which we do not have with the initial data in $(H^1(\Omega))^5$ to approximate residual operators related to derivatives within second-order spaces. At least one additional order of differentiability beyond the largest derivative order K is required to approximate ($K = 2$ for (8)), according to the principle $m \geq K + 1$ using in [15, Theorem 1.] and [9, Theorem 5.1], where m is the maximum order of derivatives used in the Sobolev norm. To ensure this additional regularity of the global solution, it is assumed in only this section that the initial data $\mathbf{U}_0 \in (H^2(\Omega))^5$. Using the same classical techniques in the proof of Proposition 3.1, we have that the associated global solution \mathbf{U} of (8) satisfies

$$\mathbf{U} \in (L^2(0, \tau; H^3(\Omega)) \cap H^2(0, \tau; L^2(\Omega)))^5.$$

Theorem 5.2 (Approximation by tanh networks). Let the solution \mathbf{U} of system 8 corresponding to the initial data $\mathbf{U}_0 \in (H^2(\Omega))^5$ satisfying

$$\mathbf{U} \in (L^2(0, \tau; H^3(\Omega)) \cap H^2(0, \tau; L^2(\Omega)))^5 =: \mathcal{X}.$$

Then for any $\varepsilon > 0$, there exists a fully connected tanh network $\mathbf{N}_\theta : \mathbb{R}^3 \rightarrow \mathbb{R}^5$ with L layers of width n satisfying

$$\min_\theta \mathcal{L}(\theta) \leq \varepsilon, \quad (87)$$

provided that n is chosen large enough. More precisely, for the continuous loss $\mathcal{R}_{\text{pde}} + \mathcal{R}_{\text{ic}} + \mathcal{R}_{\text{bc}}$:

$$\min_\theta (\mathcal{R}_{\text{pde}}(\theta) + \mathcal{R}_{\text{ic}}(\theta) + \mathcal{R}_{\text{bc}}(\theta)) \leq C_{\text{approx}} \frac{\ln^4(n)}{n^2} \|\mathbf{U}\|_{\mathcal{X}}^2, \quad (88)$$

where

$$\|\mathbf{U}\|_{\mathcal{X}}^2 := \|\mathbf{U}\|_{(L^2(0,\tau; H^3(\Omega)))^5}^2 + \|\mathbf{U}\|_{(H^2(0,\tau; L^2(\Omega)))^5}^2,$$

and C_{approx} depends on $\tau, |\Omega|$, and the system parameters ($D_T, D_B, D_O, D_I, D_S, L_F$) but is independent of θ and n .

Proof 8. The proof combines the Sobolev approximation theory for tanh networks established in [15, Theorem 1 and Corollary 2] with the structure of the residual operators 63a-63e.

Step 1 - Component-wise approximation. As explained at the beginning of the subsection, the residual operators \mathcal{R}_φ defined in 63a-63e use at most $K = 2$ derivatives (the Laplacian Δ represented by second-order spatial derivatives and ∂_t represented by a first-order temporal derivative). Therefore, to bound \mathcal{R}_{pde} in $L^2(Q)$, we must control the approximation error in the Sobolev norm $W^{K,2}(Q)$. To do this, we apply a tighter approximation bound for Sobolev-regular functions (see [15, Theorem 1] with $m = K + 1 = 3$) component-wise to each variable $\varphi \in \{T, B, O, I, S\}$. Then, there exists a tanh network $\hat{\varphi}_n$ with width parameter n such that for all $0 \leq k \leq 2$:

$$\|\varphi - \hat{\varphi}_n\|_{W^{k,2}(Q)} \leq C_{k,3,3}^{[\text{approx}]} \Delta_{k,3,3}^{[\text{tanh}]}(\delta; \alpha_{\varepsilon,\delta}) |\varphi|_{W^{3,2}(Q)}, \quad (89)$$

where the asymptotic equivalence term

$$\Delta_{k,3,3}^{[\text{tanh}]}(\delta; \alpha) \sim \left(\frac{m+d+K}{2} \right)^k \ln^k \left(\frac{1}{\delta} \right) \delta^{m-k}, \quad (90)$$

with $m = 3, d = 3, K = 2$, and $n \sim \delta^{-1}$. In our situation, the dominant asymptotic equivalence term is obtained for ($k = K = 2$). Then the terms $C_{2,3,3}^{[\text{approx}]}, \Delta_{2,3,3}^{[\text{tanh}]}(\delta)$ are given by

$$\begin{aligned} \Delta_{2,3,3}^{[\text{tanh}]}(\delta) &\sim 16 \ln^2 \left(\frac{1}{\delta} \right) \delta = 16 \frac{\ln^2(n)}{n}, \\ C_{2,3,3}^{[\text{approx}]} &\sim 2 \times 3^{9/2} (1 + \zeta) \sqrt{6} \left(\frac{3\sqrt{3}}{\pi} \right)^3. \end{aligned} \quad (91)$$

Step 2 — PDE residual bound. Since \mathbf{U} satisfies (8), the residual for each component takes the form

$$\mathcal{R}_\varphi(\mathbf{N}_\theta) = \partial_t e_\varphi - D_\varphi \Delta e_\varphi - [F_\varphi(\mathbf{U}) - F_\varphi(\hat{\mathbf{U}}_\theta)],$$

where $e_\varphi = \varphi - \hat{\varphi}_n$. Then we have:

$$\|\mathcal{R}_\varphi\|_{L^2(Q)} \leq \|\partial_t e_\varphi\|_{L^2(Q)} + D_\varphi \|\Delta e_\varphi\|_{L^2(Q)} + \|F_\varphi(\mathbf{U}) - F_\varphi(\hat{\mathbf{U}}_\theta)\|_{L^2(Q)}.$$

The first two terms are controlled by the $W^{1,2}(Q)$ and $W^{2,2}(Q)$ norm of approximation errors from Step 1. The nonlinear term is bounded by the Lipschitz estimate of Lemma 5.1:

$$\|F_\varphi(\mathbf{U}) - F_\varphi(\hat{\mathbf{U}}_\theta)\|_{L^2(Q)} \leq L_F \|\mathbf{e}\|_{(L^2(Q))^5}.$$

Therefore:

$$\begin{aligned} \mathcal{R}_{\text{pde}}(\theta) &= \int_Q \sum_{\varphi \in S} |\mathcal{R}_\varphi|^2 \, dx \, dt \\ &\leq C \sum_{\varphi \in S} \sum_{k=0}^2 \|\varphi - \hat{\varphi}_n\|_{W^{k,2}(Q)}^2. \end{aligned}$$

Applying (89) for $k = 0, 1, 2$ and using (90), we obtain

$$\mathcal{R}_{\text{pde}}(\theta) \leq C \frac{\ln^4(n)}{n^2} \sum_{\varphi \in S} \|\varphi\|_{W^{3,2}(Q)}^2. \quad (92)$$

Step 3 — IC and BC terms. By the trace Theorem, the initial condition error satisfies:

$$\begin{aligned} \mathcal{R}_{\text{ic}}(\theta) &\leq C \sum_{\varphi \in S} \|\varphi - \hat{\varphi}_n\|_{W^{1,2}(Q)}^2 \\ &\leq C \frac{\ln^2(n)}{n^4} \|\mathbf{U}\|_{(W^{3,2}(Q))^5}^2, \end{aligned}$$

which is of higher order than \mathcal{R}_{pde} . Similarly, \mathcal{R}_{bc} is controlled by the boundary trace of $\|\nabla \hat{\varphi}_n\|_{L^2(\partial\Omega)}$, bounded via the $W^{2,2}(Q)$ approximation error. Summing the three contributions yields (88).

5.2.3. Generalization: From Empirical to Continuous Loss

The PINN is trained by minimising the empirical (Monte Carlo) loss $\mathcal{L}(\theta)$ defined in (62) over finite collocation sets. We now quantify how closely $\mathcal{L}(\theta)$ approximates the true continuous functional $\mathcal{E}(\theta)$.

Let the PDE domain $Q = (0, \tau) \times \Omega$ have measure $|Q| = \tau|\Omega|$, and define the rescaled empirical estimator

$$\hat{\mathcal{E}}_{\text{pde}}(\theta) = \frac{|Q|}{N_{\text{pde}}} \sum_{k=1}^{N_{\text{pde}}} \sum_{\varphi \in \mathcal{V}} |\mathcal{R}_\varphi(x_k, t_k; \theta)|^2, \quad (93)$$

and similarly $\hat{\mathcal{E}}_{\text{ic}}, \hat{\mathcal{E}}_{\text{bc}}$ with their respective domains.

Lemma 5.2 (Monte Carlo generalization bound). Assume the residual functions $g_\varphi(z; \theta) := |\mathcal{R}_\varphi(z; \theta)|^2$ are uniformly bounded: $\sup_{z \in Q, \theta} \sum_{\varphi} |g_\varphi(z; \theta)| \leq p < \infty$. Then for any

$\delta \in (0, 1)$, with probability at least $1 - \delta$ over the random draw of N_{pde} i.i.d. uniform points in Q :

$$\left| \hat{\mathcal{E}}_{\text{pde}}(\theta) - \mathcal{E}_{\text{pde}}(\theta) \right| \leq p |Q| \sqrt{\frac{2 \ln(2/\delta)}{N_{\text{pde}}}}. \quad (94)$$

The same bound holds for $|\hat{\mathcal{E}}_{\text{ic}} - \mathcal{E}_{\text{ic}}|$ with N_{ic} and $|\Omega|$, and for $|\hat{\mathcal{E}}_{\text{bc}} - \mathcal{E}_{\text{bc}}|$ with N_{bc} and $|\Sigma| = \tau|\partial\Omega|$.

Proof 9. The rescaled estimator (93) is $\hat{\mathcal{E}}_{\text{pde}}(\theta) = |Q| \cdot \bar{g}_N$, where $\bar{g}_N = N_{\text{pde}}^{-1} \sum_k g(z_k; \theta)$ is the sample mean of the bounded random variable $g(z; \theta) = \sum_{\varphi} g_\varphi(z; \theta) \in [0, p]$.

The true functional is $\mathcal{E}_{\text{pde}}(\theta) = |Q| \cdot \mathbb{E}[g(z; \theta)]$. By Hoeffding's inequality applied to N_{pde} i.i.d. samples from $[0, p]$:

$$\mathbb{P}\left(\left|\bar{g}_N - \mathbb{E}[g]\right| \geq \sqrt{\frac{p^2 \ln(2/\delta)}{2N_{\text{pde}}}}\right) \leq \delta.$$

Multiplying by $|Q|$ gives (94).

Remark 5.2 (Convergence rate). The generalization error decreases as $\mathcal{O}(N^{-1/2})$ with respect to the number of collocation points, which is the standard Monte Carlo rate. Higher-order quasi-Monte Carlo sampling (e.g., Sobol sequences) can improve this to $\mathcal{O}((\log N)^d / N)$ (see [7]).

5.2.4. Convergence Result

Combining the conditional stability estimate (Theorem 5.1), the approximation theorem (Theorem 5.2), and the Monte Carlo generalization bound (Lemma 5.2), we arrive at the following convergence result.

Theorem 5.3 (PINN Convergence for System (8)). Let $\hat{\mathbf{U}}_{\theta^*}$ be the PINN approximation obtained by minimising $\hat{\mathcal{L}}(\theta)$ over the class of tanh networks with L layers of width n . Then for any $\delta \in (0, 1)$, with probability at least $1 - \delta$ over the random draw of collocation points:

$$\begin{aligned} \sup_{t \in [0, \tau]} \|\mathbf{U}(t) - \hat{\mathbf{U}}_{\theta^*}(t)\|_{(L^2(\Omega))^5}^2 &\leq \bar{\kappa} \left[C_{\text{approx}} \frac{\ln^4(n)}{n^2} \|\mathbf{U}\|_{\mathcal{X}}^2 \right. \\ &\quad \left. + \mathcal{G}(N_{\text{pde}}, N_{\text{ic}}, N_{\text{bc}}, \delta) \right], \end{aligned} \quad (95)$$

where $\bar{\kappa} = \bar{\kappa}(\tau, M, L_F, d_0) > 0$ is the stability constant from Theorem 5.1, independent of θ , and the generalization term is

$$\begin{aligned} \mathcal{G} &= \lambda_{\text{pde}} B |Q| \sqrt{\frac{2 \ln(2/\delta)}{N_{\text{pde}}}} + \lambda_{\text{ic}} B |\Omega| \sqrt{\frac{2 \ln(2/\delta)}{N_{\text{ic}}}} \\ &\quad + \lambda_{\text{bc}} B |\Sigma| \sqrt{\frac{2 \ln(2/\delta)}{N_{\text{bc}}}}. \end{aligned} \quad (96)$$

In particular:

- As $n \rightarrow \infty$ (wider network), the approximation term vanishes as $O(n^{-2} \ln^4(n))$.
- As $N_{\text{pde}}, N_{\text{ic}}, N_{\text{bc}} \rightarrow \infty$, the generalization term $\mathcal{G} \rightarrow 0$ at rate $O(N^{-1/2})$.
- The combined error decays as

$$O\left(\frac{\ln^4(n)}{n^2} + N^{-1/2}\right) \quad \text{as } n, N \rightarrow \infty, \quad (97)$$

where $N = \min(N_{\text{pde}}, N_{\text{ic}}, N_{\text{bc}})$.

Proof 10. From Theorem 5.1 we have:

$$\sup_{t \in [0, \tau]} \|\mathbf{e}(t)\|_{(L^2(\Omega))^5}^2 \leq \bar{\kappa} \mathcal{L}(\theta^*).$$

Decompose the continuous loss:

$$\mathcal{L}(\theta^*) = \underbrace{(\mathcal{L}(\theta^*) - \hat{\mathcal{L}}(\theta^*))}_{\text{generalisation error}} + \underbrace{\hat{\mathcal{L}}(\theta^*)}_{\text{empirical loss}}.$$

Empirical loss term. Since θ^* minimises $\hat{\mathcal{L}}$, and the approximating network θ_{approx} from Theorem 5.2 achieves $\mathcal{L}(\theta_{\text{approx}}) \leq C_{\text{approx}} n^{-2} \ln^4(n) \|\mathbf{U}\|_{\mathcal{X}}^2$:

$$\begin{aligned} \hat{\mathcal{L}}(\theta^*) &\leq \hat{\mathcal{L}}(\theta_{\text{approx}}) \\ &\leq \mathcal{L}(\theta_{\text{approx}}) + \left| \hat{\mathcal{L}}(\theta_{\text{approx}}) - \mathcal{L}(\theta_{\text{approx}}) \right| \\ &\leq C_{\text{approx}} \frac{\ln^4(n)}{n^2} \|\mathbf{U}\|_{\mathcal{X}}^2 + \mathcal{G}. \end{aligned}$$

Generalisation error term. Applying Lemma 5.1 component-wise to $\hat{\mathcal{L}}(\theta^*) - \mathcal{L}(\theta^*)$ and summing the bounds for the PDE, IC, and BC contributions gives $|\mathcal{L}(\theta^*) - \hat{\mathcal{L}}(\theta^*)| \leq \mathcal{G}$ with probability at least $1 - \delta$.

Combining the two bounds yields (95).

Using the left-hand side of the estimate (86) in Theorem 5.1, we also obtain convergence in the energy norm given by the following

Corollary 5.1. Under the same assumptions of Theorem 5.3:

$$d_0 \int_0^\tau \|\nabla \mathbf{e}(s)\|_{(L^2(\Omega))^5}^2 ds \leq \bar{\kappa} \left[C_{\text{approx}} \frac{\ln^4(n)}{n^2} \|\mathbf{U}\|_{\mathcal{X}}^2 + \mathcal{G} \right]. \quad (98)$$

Remark 5.3 (Positivity preservation). Theorem 3.1 guarantees $\mathbf{U} \geq 0$ component-wise for non-negative initial data. The network output $\hat{\mathbf{U}}_\theta$ does not automatically inherit this property. However, Theorem 5.3 implies that when $n \rightarrow \infty$ we have $\|\hat{\mathbf{U}}_{\theta^*} - \mathbf{U}\|_{L^\infty(0, \tau; (L^2(\Omega))^5)} \rightarrow 0$, so the negative part norm $\|\hat{\mathbf{U}}_{\theta^*}^-\|_{(L^2(\Omega))^5} \leq \|\mathbf{e}\|_{(L^2(\Omega))^5} \rightarrow 0$ as well when $n \rightarrow \infty$.

6. Numerical Results

This section tests the proposed PINN framework with thorough numerical experiments on the five-species tumor-bacteria system (8) in a domain $\Omega \in \mathbb{R}^2$ representing the tissue. We show that the trained network effectively captures the spatiotemporal dynamics introduced by the mathematical analysis in previous sections. We also confirm the four-phase therapy progression mentioned in the abstract: initial tumor growth, hypoxia bacterial activation, quorum-sensing mediated tumor suppression, and coexistence. For the code and other details, please refer to our repository¹

6.1. Implementation Details

The neural network architecture is employed a fully connected feedforward network with architecture [3, 64, 64, 64, 64, 5]. This architecture is comprising four hidden layers of 64 neurons each with tanh activation, and a linear output layer producing the five state variables $\hat{\mathbf{U}} = (\hat{T}, \hat{B}, \hat{O}, \hat{I}, \hat{S})^\top$. The network has 21,829 trainable parameters and processes spatio-temporal coordinates $(x, y, t) \in [0, 6] \times [0, 6] \times [0, 30]$ as input.

For the collocation points Training data consists of $N_{\text{pde}} = 10,000$ interior points sampled uniformly over $Q = (0, 30) \times \Omega$, $N_{\text{ic}} = 600$ initial condition points at $t = 0$, and $N_{\text{bc}} = 400$ boundary points on $\partial\Omega \times (0, 30)$. The full dataset is partitioned 60%, 20%, 20% into training, validation, and test subsets following standard practice.

Remark 6.1. In the loss functions, we set $\lambda_{\text{ic}} = 50.0$ to enforce initial condition fidelity, while $\lambda_{\text{pde}} = 1.0$ and $\lambda_{\text{bc}} = 1.0$. This weighting prevents collapse to the trivial solution $\mathbf{U} \equiv 0$. It also makes sure the network follows the specified Gaussian tumor seed and bacterial inoculum.

Neural network parameters are optimised by the Adam algorithm [26], with an initial learning rate of $\eta_0 = 10^{-3}$. *ReduceLROnPlateau* decays this rate with a factor of 0.5 and patience of 1000 epochs. Overfitting can be avoided by stopping early and being patient for $P = 2000$ epochs. The size of the mini-batch is 512. All calculations are carried out on the Tesla T4 15 Go using PyTorch 2.0. Early stopping with patience P epochs prevents overfitting. The full procedure is summarised in Algorithm 1.

All parameters entering system (8) are calibrated from peer-reviewed experimental and computational literature. Table 1 provides a complete listing.

6.2. Training

The training history in Figure 2 demonstrates successful PINN optimization across all loss components. The network converges to a best validation loss of $\mathcal{L}_{\text{val}}^{\text{best}} \approx 1.2 \times 10^{-3}$ at epoch 7894, demonstrating stable optimization without overfitting. The Total composite loss decreases from $\sim 10^3$ to $\mathcal{O}(10^{-3})$ with training (blue) and validation (orange) curves tracking closely, indicating good generalization. Moreover, PDE residual loss exhibits monotonic decay from $\sim 10^2$ to

¹<https://github.com/FARKANE/-Tumor-Bacterial-Therapy-PINNs>

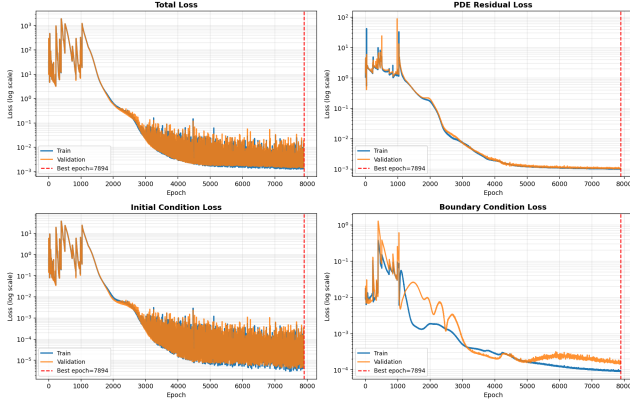


Figure 2: Training and validation loss evolution over 8000 epochs.

1.1×10^{-3} , confirming that the network learns to satisfy the five coupled reaction-diffusion equations. Additionally, initial condition loss drops sharply in the first 2000 epochs from $\sim 10^1$ to $\mathcal{O}(10^{-5})$ due to the high weighting $\lambda_{ic} = 50.0$, confirming strong adherence to the prescribed Gaussian profiles. The last sub-figure represents shows that boundary condition loss decreases from $\sim 10^0$ to $\mathcal{O}(10^{-4})$, validating enforcement of the zero-flux Neumann conditions. The red dashed line marks the best epoch (7894) where early stopping is triggered.

6.3. Results and Discussion

Figure 3 shows the complete spatiotemporal dynamics of bacterial cancer therapy as described by the trained PINN. This presents evolution of the five-species tumor-bacteria system over 30 days on the $6 \times 6 \text{ mm}^2$ tissue domain. Each row corresponds to a temporal snapshot at $t \in \{0, 5, 10, 15, 20, 25, 30\}$ days; columns show tumor density T (red), bacterial density B (blue), oxygen O (green), immunosuppressive cytokines I (orange), and quorum-sensing signal S (purple).

The PINN solution was sampled at fixed spatial locations over time to ensure a thorough analysis of the experiments. The coordinates for these locations are provided in Table 2.

The solution demonstrates four therapeutic stages: (I) tumor growth reaching $T_{\max} \approx 0.96$ by $t = 5$ days; (II) tumor decrease to $T \approx 0.05$ in spite of low bacterial density ($B \sim 0.04\text{--}0.09$); (III) accumulation of signals ($S \approx 0.05\text{--}0.07$) facilitating ongoing tumor cells suppression; (IV) a nearly tumor-free condition ($T \approx 0.01$, $B \approx 0.04$) by $t = 30$ days. Oxygen levels stay close to baseline ($O \approx 0.19\text{--}0.20$) throughout the process, while cytokines correspond to tumor density.

The solution has four clear phases: **Phase I (0-5 days): Tumor expansion.** At the beginning, the tumor variable T is at its maximum value ($T_{\max} \approx 0.96$). The bacteria (B_0), introduced slightly away from the tumor center, begin to grow and move toward the tumor. Even though the tumor consumes oxygen rapidly, the oxygen level O stays relatively stable near the vascular value ($O_{\text{vas}} \approx 0.20$) because the

vascular supply is high.

Phase II (5-15 days): The tumor gets smaller. Even though the bacteria load is low and the oxygen levels are normal, the tumor density drops sharply from $T \approx 0.96$ to $T \approx 0.05$. This is because of natural tumor cell death ($\delta_T T$), carrying capacity saturation, and the start of quorum-sensing suppression ($-\alpha_S S T$). Bacterial density levels off at $B \approx 0.04$, which is the right amount for immune clearance ($\beta_I I B$) to keep up with oxygen-modulated growth. The QS signal starts to build up ($S \approx 0.05\text{--}0.07$) and spreads from the bacterial site to the tumor center. This activates the cytotoxic term $-\alpha_S S T \approx -0.01T$.

Phase III (15-25 days): QS-mediated suppression. Tumor density continues decreasing ($T \approx 0.05 \rightarrow 0.01$) as the stabilized signal ($S \approx 0.05$) maintains suppression. Bacteria reach a plateau at $B \approx 0.04$ in a state of quasi-equilibrium, where production ($\approx 0.167B$) balances clearance ($\approx 0.106B$). Cytokines decay proportionally to tumor ($I \approx 0.03 \rightarrow 0.01$), reducing immune pressure on residual bacteria.

Phase IV (>25 days): Near-tumor-free coexistence. The system approaches a low-density equilibrium: $(T, B, O, I, S) \approx (0.01, 0.04, 0.19, 0.01, 0.05)$, which corresponds to a near stable tumor-free equilibrium (Proposition 3.2) rather than complete eradication. Persistent bacteria act as a reservoir for QS signals, stopping tumors from growing back even when the immune system isn't as strong.

The Figure 4 illustrates the tumor dynamics throughout the 30-day therapy. In panel (a), the domain-averaged tumor density rises to an early maximum before entering a steady, monotonic decline. At the same time, the variability bands progressively narrow, reflecting increasing spatial uniformity as the tumor regresses. Panel (b) depicts the overall tumor burden. A short-lived initial growth phase (highlighted in red) precedes an extended degradation period (shown in green), clearly illustrating the therapeutic impact of the bacterial intervention. Panel (c) emphasizes spatial heterogeneity. The tumor center undergoes the most pronounced regression, whereas monitoring points near the boundaries remain close to baseline levels, confirming that the tumor remains confined within the computational domain.

The spatial snapshots in the bottom row (d1-d3) provide a visual summary of this progression. The tumor begins as a concentrated Gaussian-like core, transitions into a more diffuse intermediate configuration during therapy, and ultimately approaches a nearly uniform low-density residual state by the end of treatment.

Figure 5 shows how tumors interact with bacteria and the outcomes of treatments. Panel (a) illustrates that as the tumor (red) decreases in size, bacteria (blue dashed) initially decline but then stabilize at moderate levels. This indicates that a high number of bacteria isn't necessary for effectiveness. Panel (b) depicts the system from a state of high tumor/low bacteria (green circle) to significant tumor shrinkage while bacteria levels remain moderate (red star) over a period of 30 days. Panel (c) illustrates that the bacteria-to-tumor

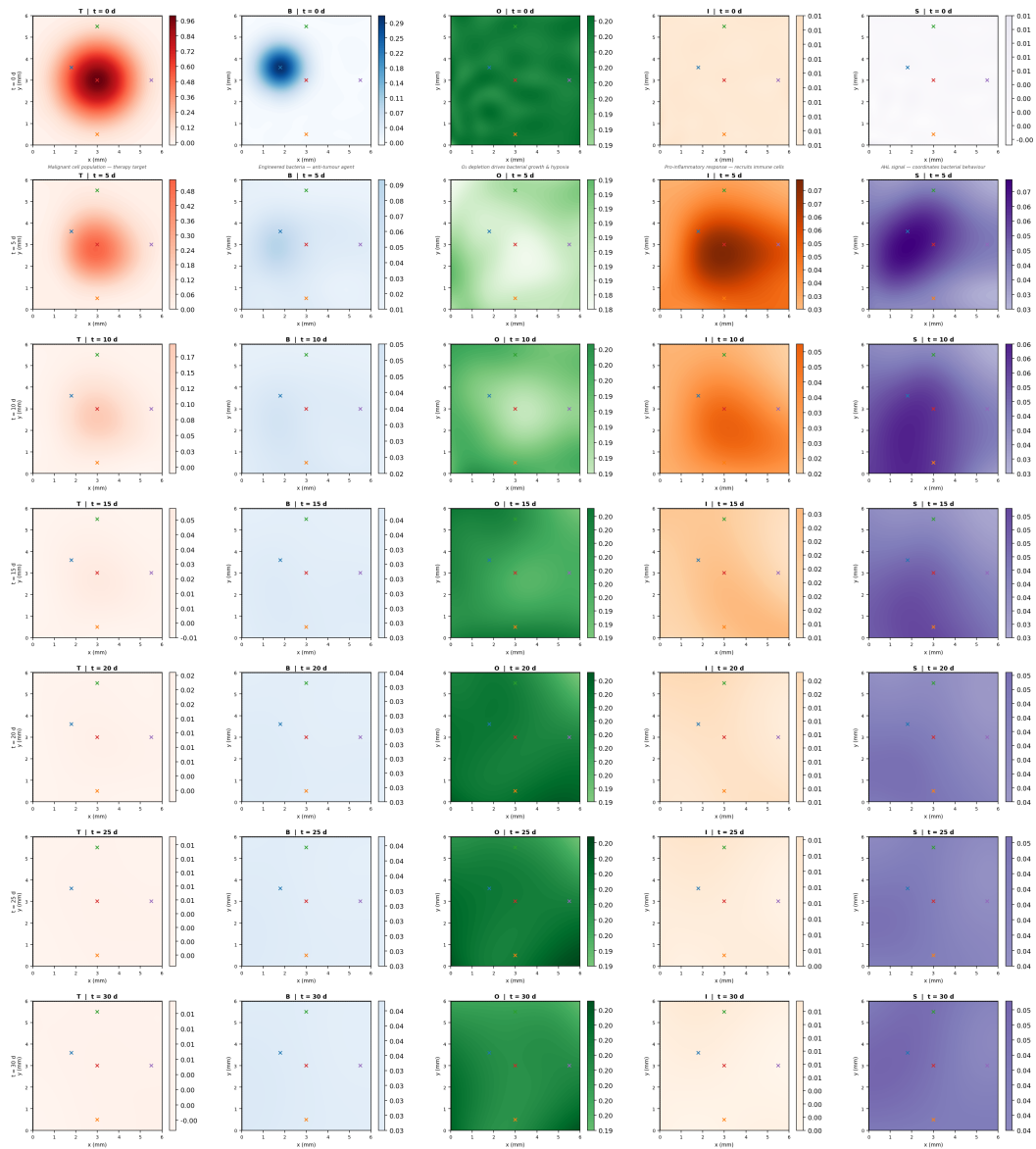


Figure 3: Spatio-temporal evolution of the five-species tumor-bacteria system over 30 days.

Table 2
Monitoring Probe Locations in Figure 1

Symbol	Color	Location (x, y)	Purpose
×	Red	(3.0, 3.0)	Tumor center-initial tumor seed location
×	Blue	(1.8, 3.6)	Bacteria injection site, 30% x, 60% y of domain
×	Green	(3.0, 5.5)	Top edge, Near-boundary monitoring point
×	Orange	(3.0, 0.5)	Bottom edge, Near-boundary monitoring point
×	Purple	(5.5, 3.0)	Right edge, Near-boundary monitoring point

ratio peaks when the tumor is small enough. This indicates the effective treatment. Panels (d) and (e) depict spatial dynamics. The greatest tumor reduction occurs at the center, while bacteria tend to stay close to their injection site. Panel (f) shows that bacteria can be located far from the tumor. Diffusible signals prompt the treatment effect. This aligns

with clinical cases where Salmonella act on tumor edges through released molecules instead of direct contact.

Figure 6 shows that oxygen levels remain mostly normal during the treatment. This is different from many bacterial therapies that depend on low-oxygen (hypoxia) tumor regions. In panel (a), oxygen slightly drops during the first

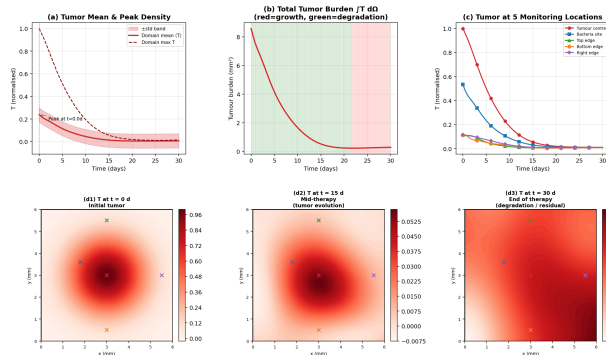


Figure 4: Tumor cell dynamics: growth phase, peak and bacterial-driven degradation

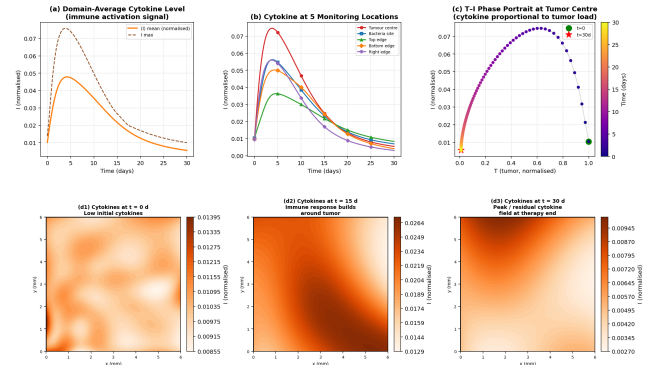


Figure 7: Immune cytokine response (I). Cytokines are produced by tumor cells and regulate immune activity.

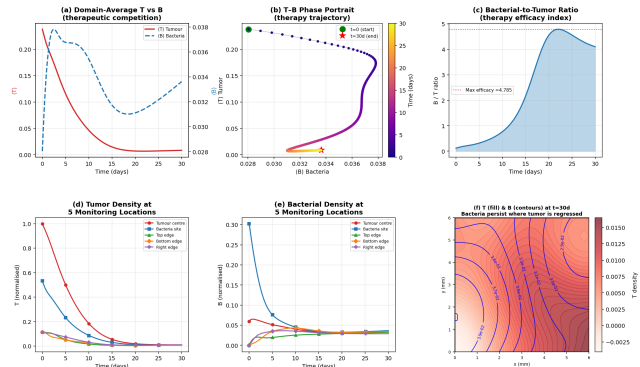


Figure 5: Bacterial therapy effect: Salmonella-tumor interaction dynamics bacteria colonise hypoxia regions, produce signals, and drive tumors regression.

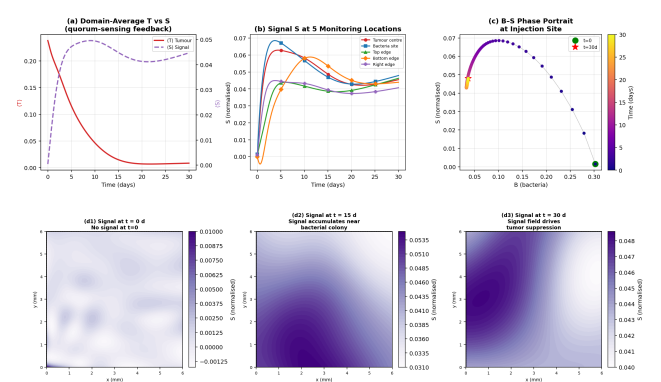


Figure 8: Bacterial quorum-sensing signal (S) dynamics.

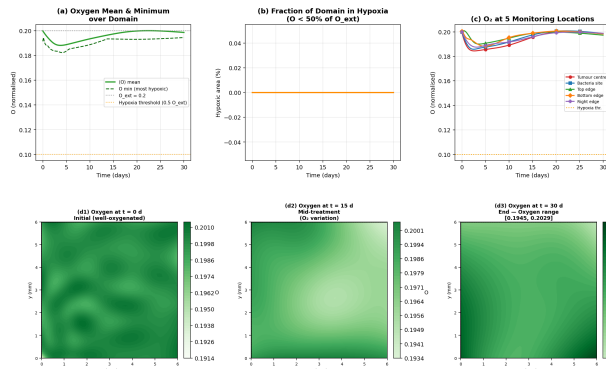


Figure 6: Oxygen depletion & hypoxia dynamics, O_2 consumed by tumor.

five days. This happens because the tumor is still large and consumes more oxygen. After treatment begins, oxygen levels gradually return to the vascular baseline ($O_{vas} \approx 0.20$) as the tumor becomes smaller.

Panel (b) confirms that the environment stays stable. The hypoxia fraction remains essentially zero during the entire 30-day period. Panel (c) and the spatial snapshots (d1–d3) show a similar pattern. Oxygen stays well distributed across the tissue, with no strong gradients. Overall, these results

suggest that the treatment does not rely on low-oxygen conditions. Instead, tumor suppression is mainly driven by the diffusion of quorum-sensing signals released by the bacteria, rather than by hypoxia-dependent bacterial colonization.

Figure 7 shows the host inflammatory response to the tumor. Panel (a) shows cytokine levels rising sharply around days 4–5. This matches the time when the bacteria and the large tumor interact most strongly. After the peak, cytokines fall steadily as the tumor is reduced. Panel (b) shows the response is local. The tumor center has much higher cytokine levels than areas farther away. Panels (d1–d3) make this clear: cytokines build up around the tumor (d2) and then fade to a low background by the end (d3). Panel (c) represents the phase portrait. Cytokines rise as the tumor shrinks, then drop back to near zero once the tumor is gone. In short, the cytokines response is driven by the tumor. It peaks during active treatment and then settles down as the malignancy is cleared.

Figure 8 shows how quorum-sensing signals play a key role in tumor suppression. Panel (a) illustrates an inverse relationship over time: as the tumor density decreases steadily, the signal concentration increases and levels off, creating a feedback loop that helps maintain treatment effectiveness. Panel (b) displays signal buildup at all observed sites, with the highest levels found at the bacteria injection point and the center of the tumor. This suggests that diffusion helps

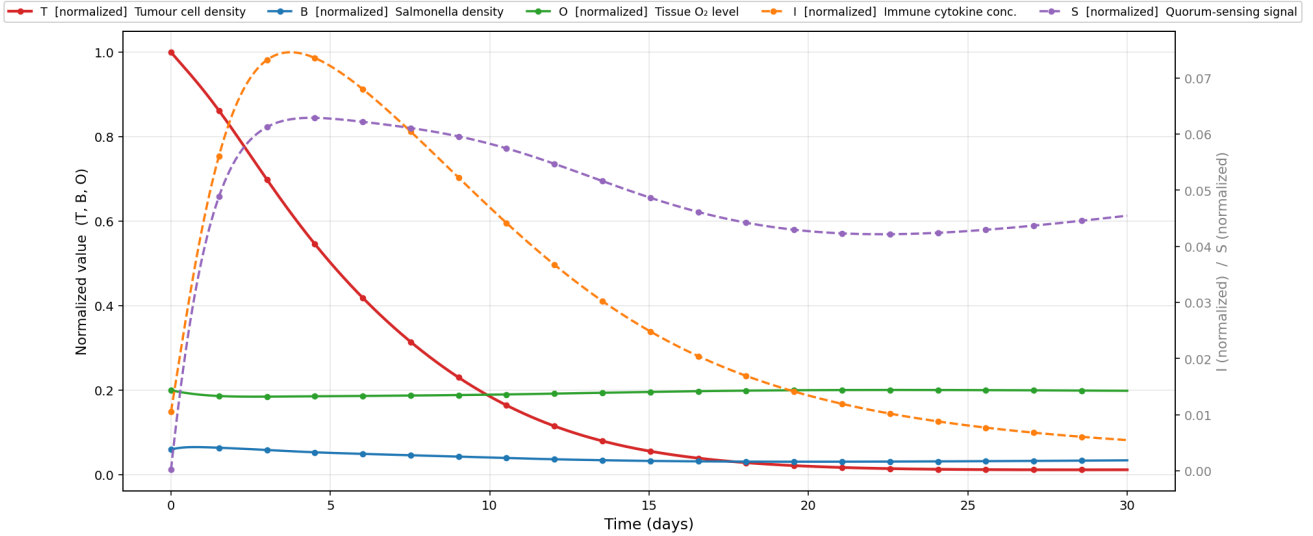


Figure 9: All 5 variables at fixed $(x = 3.0, y = 3.0)$: solid lines represent (T, B, O) normalized, dashed lines represent (I, S) normalized).

connect the bacterial source to the distant tumor target. The B-S phase portrait in panel (c) tracks how signals are produced at the injection site. There is a quick buildup during the early establishment of bacteria, followed by a stable plateau as the bacteria settle at a moderate density, indicating that quorum activation depends on density. The spatial snapshots in panels (d1-d3) highlight the essential treatment mechanism—signals spread from the bacterial colony like a purple cloud, reaching the entire area, including the tumor site, where they trigger the suppression term $-\alpha_S ST$. This action from a distance supports the main idea of the model: bacteria do not need to invade the tumor mass directly. Instead, diffusible AHL molecules manage the therapeutic effects from afar, leading to lasting tumor reduction through molecular communication rather than direct bacterial damage.

Figure 9 shows how all five state variables change over time at the tumor-centered probe $(x, y) = (3.0, 3.0)$ mm during the 30-day treatment. Tumor density T decreases from $T_0 \approx 1.0$ to a residual $T \approx 0.01$. This decline results from the combined effects of apoptosis, saturation of carrying capacity, and quorum-sensing suppression $-\alpha_S ST$. Bacterial density B levels off at a quasi-equilibrium plateau $B^* \approx 0.04$, where oxygen-modulated growth balances immune clearance and natural death, allowing continuous AHL production even after the active regression period. Oxygen O stays at the vascular baseline $O_{\text{vas}} = 0.20$ throughout, confirming tissue normoxia and indicating a molecular rather than hypoxia treatment mechanism. Cytokines I reach their peak at $t \approx 5$ days, directly linked to the maximum tumor burden, and then decline, consistent with the production term $\beta_T T$. The quorum-sensing signal S increases quickly, stabilizes at $S \approx 0.045$, and continues to suppress the tumor remotely through diffusion. Notably, S peaks just before the sharpest tumor decline, highlighting the causal role of quorum-sensing in tumor regression. The final state

$(T, B, O, I, S) \approx (0.01, 0.04, 0.19, 0.01, 0.05)$ agrees with the predicted coexistence equilibrium.

6.4. Discussion

The numerical experiments confirm the proposed PINN framework. The trained network generates solutions that are non-negative, bounded, and spatially smooth, aligning with mathematical analysis. The composite validation loss drops to $\mathcal{L}_{\text{val}}^{\text{best}} \approx 1.2 \times 10^{-3}$ at epoch 7894, with training and validation curves closely tracking each other, showing generalization without overfitting. The final state matches the analytically determined coexistence equilibrium, offering direct empirical support for the steady-state analysis described in Section 3.3.

A key finding is that tumor suppression occurs under normal oxygen conditions. The therapeutic effect is driven by diffusible quorum-sensing signals. It is not driven by hypoxia-induced bacterial activation. The model shows a spatial separation. Bacteria remain at the injection site. The distant tumor is almost completely eliminated. This indicates that long-range molecular communication is the main cytotoxic mechanism. These results agree with experimental data on Salmonella-based therapies in well-vascularized tissue [21]. Overall, the results show that the PINN framework describes the four-phase spatio-temporal dynamics of the tumor microenvironment. The simulations are performed on a 6×6 mm² domain. This provides empirical support for the convergence guarantees stated in Theorem 5.3.

7. Conclusion

This paper presents a mathematical and computational framework for modeling bacterial cancer therapy. The model is based on a system of five coupled nonlinear reaction-diffusion equations. These equations describe the cross-interaction between tumor density, bacterial colonization,

oxygen concentration, immunosuppressive cytokines, and quorum-sensing signals. Four main contributions were established. First, we formulated a coupled reaction-diffusion system. It describes hypoxia-driven bacterial activation, quorum-sensing-mediated tumor suppression, vascular oxygen exchange, and tumor-induced immunosuppressive cytokines production. To our knowledge, these interactions had not been jointly modeled in a single PDE framework. Second, we provided a mathematical analysis. Third, we developed a convergence theory for the PINN approximation. This result extends existing PINN convergence guarantees to five coupled nonlinear reaction–diffusion equations describing tumor tissue systems. Fourth, various simulations were conducted for different experiments, as well as a parameter sensitivity analysis.

Several directions remain for future work. From a modeling perspective, more realistic features can be added. Nonlinear boundary conditions could describe tumor invasion into surrounding tissue. Stochastic perturbations could describe patient-specific variability. The model could also be coupled with pharmacokinetic models for combination therapies. From a computational perspective, improvements are possible. Adaptive collocation strategies could be used. Domain decomposition could help handle large three-dimensional geometries. Patient imaging data could be included as initial or boundary conditions. From a theoretical side, more accurate approximation bounds are needed. Methods such as quasi-Monte Carlo sampling or adaptive network architectures could help. The optimization error in the convergence analysis also remains a challenge.

Finally, while the signaling molecule S contributes to sustained tumor suppression, prolonged signal persistence may induce chronic immune activation or off-target cytotoxic effects, warranting further investigation through extended-horizon simulations and experimental validation.

A. Biological Parameters Sensitivity

In this section, we analyze the model’s sensitivity to some biological parameters, specifically α_S , β_I , and γ_{vas} (Figure 10).

We first examined how the α_S influences the system (see Figure 10a). When this parameter is small (e.g., 0.01), the tumor density T slowly decreases and stabilizes at a low level. However, when α_S becomes larger (such as 0.50), shown by the cyan dashed line), the tumor is suppressed more strongly at the beginning but eventually stabilizes at a higher level. This means the response is not purely linear: strong inhibition at first increases oxygen levels O , which improves the tumor’s metabolic conditions and allows it to recover instead of being fully eliminated.

At the same time, higher values of α_S lead to a larger bacterial population B and a stronger inhibitory signal S . Even though this signal suppresses the tumor, it is not strong enough to fully overcome the tumor’s ability to adapt, especially in the presence of higher cytokine I and oxygen O levels. Therefore, choosing an appropriate value of α_S is

important to maximize tumor suppression without allowing the system to settle into a persistent tumor state.

Next, we focused on β_I (the immune clearance rate), as it serves as a critical threshold for treatment success (Figure 10b). The sensitivity analysis of the parameter β_I , which describes cytokine-related interactions affecting the bacterial density, shows that increasing this parameter generally increases the overall activity of the system. When β_I increases from 0.05 to 1.00, both the bacterial density B and the inhibitory signal S become stronger. This means that higher values of β_I allow the therapeutic bacteria to persist and grow more in the system.

However, this stronger bacterial presence does not necessarily improve the treatment outcome. In fact, the tumor density T settles at a slightly higher level when $\beta_I = 1.00$ (cyan dashed line) compared with lower values. In other words, having more bacteria and a stronger inhibitory signal does not always lead to better tumor suppression.

One possible explanation is that the therapeutic signal S and the final tumor suppression become partly disconnected. This is suggested by the oxygen profiles O , which remain almost the same for all parameter values. At higher β_I , the cytokine level I also increases, which may create a balanced state where the tumor adapts to the stronger inhibition. As a result, the system reaches a kind of saturation point: even though more bacteria are present, they no longer improve tumor elimination. This shows that choosing the right parameter range is more important than simply increasing the bacterial concentration.

Finally, we studied how the vascular oxygen supply rate γ_{vas} affects the treatment outcome. This is shown in Figure 10c. When γ_{vas} increases from 0.01 to 0.50, the oxygen level O in the tissue rises, changing the environment from hypoxia (low oxygen) to normoxia (normal oxygen). As oxygen becomes more available, the tumor density T grows again and reaches much higher steady levels, especially at high supply rates (e.g., 0.50). The larger tumor mass also produces more cytokines I , leading to a highly active state where tumor growth eventually overcomes the therapeutic effect.

The effectiveness of the therapy also depends on how oxygen affects the anaerobic bacteria B . Although stronger vascularization causes a larger initial peak in bacterial density, the long-term bacterial levels and the inhibitory signal S they produce, become much lower when γ_{vas} is high. This reduces the pressure on the tumor over time and allows it to grow again. In other words, higher vascularization is a double-edged sword: it can initially help the bacteria grow, but the higher oxygen levels eventually prevent them from surviving. These results suggest that maintaining hypoxia regions in the tumor, or using bacteria that tolerate oxygen better, may be necessary for long-lasting tumor control.

In summary, the simulations show that the success of bacteria-based tumor therapy depends on a delicate balance between the immune response of the host and the metabolic conditions inside the tumor. Increasing the inhibitory effect

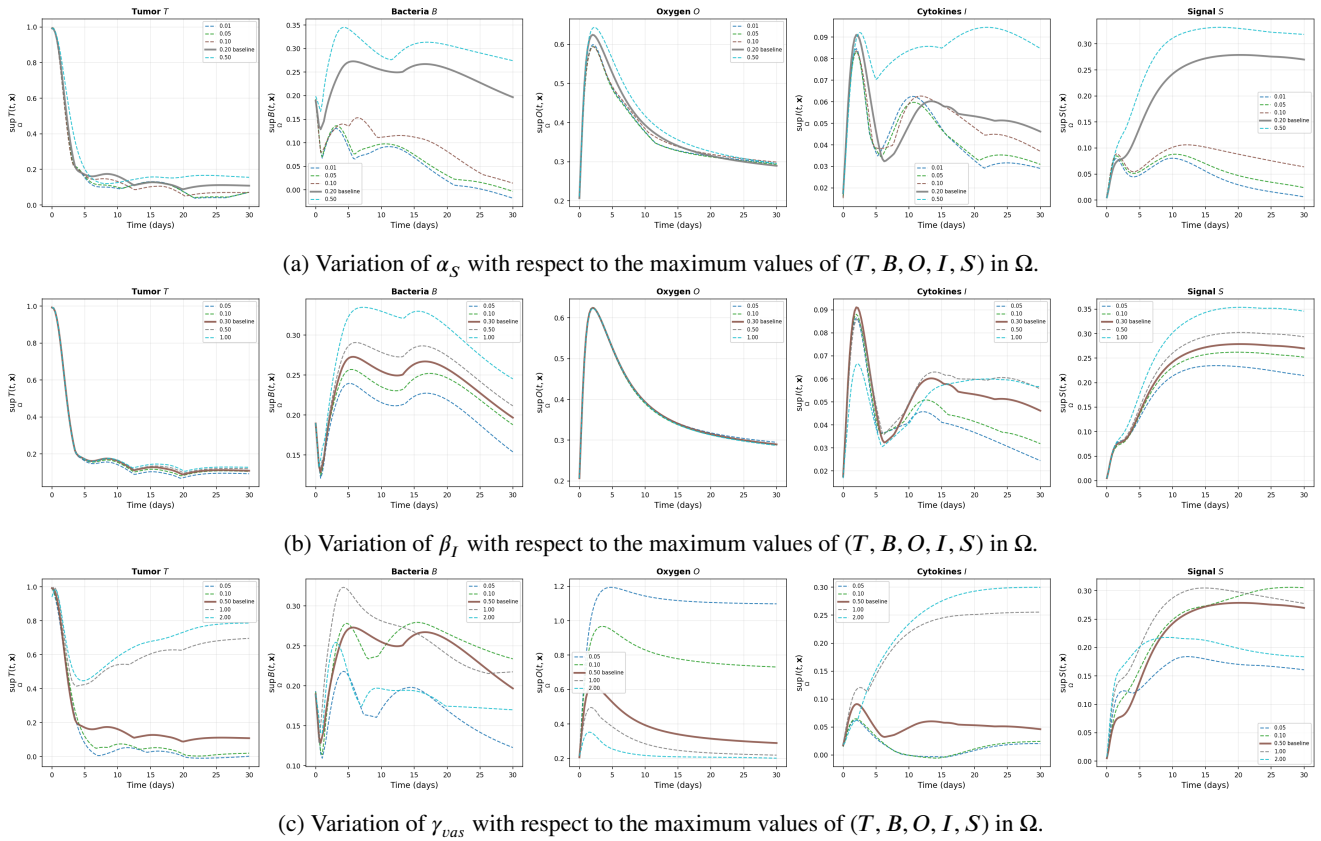


Figure 10: Sensitivity of the model to the specific parameters α_S , β_I , and γ_{vas} .

or the oxygen supply can improve the treatment at the beginning, but it may also activate feedback mechanisms. For example, cytokines can clear the bacteria too quickly, and higher oxygen levels can reduce the survival of anaerobic bacteria. Both effects can allow the tumor to grow again or persist in the system.

References

- [1] Ram Prasad Aganja, Chandran Sivasankar, and John Hwa Lee. Ai-2 quorum sensing controlled delivery of cytolysin-a by tryptophan auxotrophic low-endotoxic salmonella and its anticancer effects in ct26 mice with colon cancer. *Journal of Advanced Research*, 61:83–100, 2024.
- [2] Taghreed H Alarabi, Nasser S Elgazery, and Asmaa F Elelmy. Mathematical model of oxytactic bacteria's role on mhd nanofluid flow across a circular cylinder: application of drug-carrier in hypoxic tumour. *Journal of Taibah University for Science*, 16(1):703–724, 2022.
- [3] Brittany N Balhouse, Logan Patterson, Eva M Schmelz, Daniel J Slade, and Scott S Verbridge. N-(3-oxododecanoyl)-l-homoserine lactone interactions in the breast tumor microenvironment: Implications for breast cancer viability and proliferation in vitro. *PLoS One*, 12(7):e0180372, 2017.
- [4] Andrew R Barron. Approximation and estimation bounds for artificial neural networks. *Machine learning*, 14(1):115–133, 1994.
- [5] Aziz Belmiloudi. Mathematical modeling and optimal control problems in brain tumor targeted drug delivery strategies. *International Journal of Biomathematics*, 10(04):1750056, 2017.
- [6] Susanne C Brenner and L Ridgway Scott. *The mathematical theory of finite element methods*. Springer, 2008.
- [7] Russel E Caffisch. Monte carlo and quasi-monte carlo methods. *Acta numerica*, 7:1–49, 1998.
- [8] Tim De Ryck, Ameya D Jagtap, and Siddhartha Mishra. Error estimates for physics-informed neural networks approximating the navier–stokes equations. *IMA Journal of Numerical Analysis*, 44(1):83–119, 2024.
- [9] Tim De Ryck, Samuel Lanthaler, and Siddhartha Mishra. On the approximation of functions by tanh neural networks. *Neural Networks*, 143:732–750, 2021.
- [10] Raluca Eftimie and Charlotte Barelle. Mathematical investigation of innate immune responses to lung cancer: The role of macrophages with mixed phenotypes. *Journal of Theoretical Biology*, 524:110739, 2021.
- [11] Walid El Afari, Mohammed Ziani, and Fatna Assaoui. Tumor propagation modeling using physics-informed neural networks and variational methods for mri image segmentation. *Journal of Mathematical Imaging and Vision*, 68(2):8, 2026.
- [12] Ayoub Farkane, Mohamed Boutayeb, Mustapha Oudani, and Mounir Ghogho. An adaptive physics-informed neural network observer for state estimation in nonlinear dynamical systems. *Engineering Applications of Artificial Intelligence*, 162:112655, 2025.
- [13] Ayoub Farkane, Mounir Ghogho, Mustapha Oudani, and Mohamed Boutayeb. Enhancing physics informed neural networks for solving navier–stokes equations. *International Journal for Numerical Methods in Fluids*, 96(4):381–396, 2024.
- [14] A. Geretovszky and G. Röst. A mathematical model for cancer dynamics with treatment and saboteur bacteria. *bioRxiv*, pages 1–19, 2025.
- [15] Benjamin Girault, Rémi Emonet, Amaury Habrard, Jordan Patracone, and Marc Sebban. Approximation error of sobolev regular functions with tanh neural networks: theoretical impact on pinns. In *Joint European Conference on Machine Learning and Knowledge Discovery*

- in *Databases*, pages 266–282. Springer, 2024.
- [16] Xavier Glorot, Antoine Bordes, and Yoshua Bengio. Deep sparse rectifier neural networks. In *Proceedings of the fourteenth international conference on artificial intelligence and statistics*, pages 315–323. JMLR Workshop and Conference Proceedings, 2011.
- [17] Ingo Gühring and Mones Raslan. Approximation rates for neural networks with encodable weights in smoothness spaces. *Neural Networks*, 134:107–130, 2021.
- [18] Yufei Guo, Mengxue Gao, Lina Wang, Haibin Yuan, Jianan Yin, Jiahao Wu, Xinran Gao, Zhixin Zhu, Yan Zhang, Zichen Wang, et al. An engineered probiotic consortium based on quorum-sensing for colorectal cancer immunotherapy. *Advanced Science*, 12(46):e12744, 2025.
- [19] D. Hanahan. Hallmarks of cancer: new dimensions. *Cancer discovery*, 12(1):31–46, 2022.
- [20] Kurt Hornik. Some new results on neural network approximation. *Neural networks*, 6(8):1069–1072, 1993.
- [21] Lars M Howell and Neil S Forbes. Mathematical modeling of salmonella cancer therapies demonstrates the necessity of both bacterial cytotoxicity and immune activation. *Bioengineering*, 12(7):751, 2025.
- [22] Angela M Jarrett, David A Hormuth, Stephanie L Barnes, Xinzeng Feng, Wei Huang, and Thomas E Yankeelov. Incorporating drug delivery into an imaging-driven, mechanics-coupled reaction diffusion model for predicting the response of breast cancer to neoadjuvant chemotherapy: theory and preliminary clinical results. *Physics in Medicine & Biology*, 63(10):105015, 2018.
- [23] Angela M Jarrett, Ernesto ABF Lima, David A Hormuth, Matthew T McKenna, Xinzeng Feng, David A Ekrut, Anna Claudia M Resende, Amy Brock, Thomas E Yankeelov, et al. Mathematical models of tumor cell proliferation: A review of the literature. *Expert review of anticancer therapy*, 18(12):1271, 2018.
- [24] X. Jing, F. Yang, and C. Shao. Role of hypoxia in cancer therapy by regulating the tumor microenvironment. *Molecular cancer*, 18:157, 2019.
- [25] Venkatachalam Kandasamy, Vladimir Simic, Nebojsa Bacanin, and Dragan Pamucar. Optimized deep learning networks for accurate identification of cancer cells in bone marrow. *Neural Networks*, 181:106822, 2025.
- [26] Diederik P Kingma and Jimmy Ba. Adam: A method for stochastic optimization. *arXiv preprint arXiv:1412.6980*, 2014.
- [27] Ioannis Lampropoulos, Panayotis G Kevrekidis, Christos E Zois, Helen Byrne, and Michail Kavousanakis. Spatio-temporal dynamics of m1 and m2 macrophages in a multiphase model of tumor growth: I. lampropoulos et al. *Bulletin of Mathematical Biology*, 87(7):92, 2025.
- [28] David Lassounon, Aziz Belmiloudi, and Mounir Haddou. Optimal control problem in treatment strategies for breast tumors. In *International Conference on Optimization and Applications*, pages 293–307. Springer, 2024.
- [29] David Lassounon, Aziz Belmiloudi, and Mounir Haddou. A penalization approach in breast cancer chemotherapy: Preliminary numerical simulations. In *2024 10th International Conference on Optimization and Applications (ICOA)*, pages 1–6. IEEE, 2024.
- [30] J-L Lions. " quelques méthodes de résolution des problèmes aux limites non-linéaires,". *Dunod*, 1969.
- [31] Guillermo Lorenzo, David A. Hormuth, Angela M. Jarrett, Ernesto A.B.F. Lima, Shashank Subramanian, George Biros, J. Tinsley Oden, Thomas Joseph Robert Hughes, and Thomas E. Yankeelov. Quantitative in vivo imaging to enable tumor forecasting and treatment optimization. *ArXiv*, abs/2102.12602, 2021.
- [32] Pietro Mascheroni, Michael Meyer-Hermann, and Haralampos Hatzikirou. Investigating the physical effects in bacterial therapies for avascular tumors. *Frontiers in Microbiology*, 11:1083, 2020.
- [33] Edoardo Milotti, Thierry Fredrich, Roberto Chignola, and Heiko Rieger. Oxygen in the tumor microenvironment: mathematical and numerical modeling. *Tumor Microenvironment: Molecular Players–Part A*, pages 53–76, 2020.
- [34] Siddhartha Mishra and Roberto Molinaro. Estimates on the generalization error of physics-informed neural networks for approximating pdes. *IMA Journal of Numerical Analysis*, 43(1):1–43, 2023.
- [35] James Dickson Murray and James Dickson Murray. *Mathematical biology: II: spatial models and biomedical applications*, volume 18. Springer, 2003.
- [36] Manuel Arturo Nova-Martínez and Héctor Andrés Granada-Díaz. Tumor expansion and immune regulation in a mathematical model of cancer under variations in tumor cell proliferation rate and innate immune stimulation. *Mathematical Biosciences and Engineering*, 22(11):2826–2851, 2025.
- [37] Zheng Pang, Meng-Di Gu, and Tong Tang. Pseudomonas aeruginosa in cancer therapy: current knowledge, challenges and future perspectives. *Frontiers in Oncology*, 12:891187, 2022.
- [38] Adam Paszke, Sam Gross, Francisco Massa, Adam Lerer, James Bradbury, Gregory Chanan, Trevor Killeen, Zeming Lin, Natalia Gimelshein, Luca Antiga, et al. Pytorch: An imperative style, high-performance deep learning library. *Advances in neural information processing systems*, 32, 2019.
- [39] Michel Pierre. Global existence in reaction-diffusion systems with control of mass: a survey. *Milan Journal of Mathematics*, 78(2):417–455, 2010.
- [40] Daniela F Quail and Johanna A Joyce. Microenvironmental regulation of tumor progression and metastasis. *Nature medicine*, 19(11):1423–1437, 2013.
- [41] Maziar Raissi, Paris Perdikaris, and George E Karniadakis. Physics-informed neural networks: A deep learning framework for solving forward and inverse problems involving nonlinear partial differential equations. *Journal of Computational physics*, 378:686–707, 2019.
- [42] José Alberto Rodrigues. Using physics-informed neural networks (pinns) for tumor cell growth modeling. *Mathematics*, 12(8):1195, 2024.
- [43] Gopinath Sadhu, KS Yadav, Siddhartha Sankar Ghosh, and DC Dalal. On impact of oxygen distribution on tumor necrotic region: a multi-phase model. *arXiv preprint arXiv:2311.03394*, 2023.
- [44] Behrouz Ebadí Sharafabad, Asghar Abdoli, Parisa Jamour, and Azita Dilmaghani. The ability of clostridium novyi-nt spores to induce apoptosis via the mitochondrial pathway in mice with hpv-positive cervical cancer tumors derived from the tc-1 cell line. *BMC Complementary Medicine and Therapies*, 24(1):427, 2024.
- [45] Yeonjong Shin, Jerome Darbon, and George Em Karniadakis. On the convergence of physics informed neural networks for linear second-order elliptic and parabolic type pdes. *arXiv preprint arXiv:2004.01806*, 2020.
- [46] Isabelle Soerjomataram and Freddie Bray. Planning for tomorrow: global cancer incidence and the role of prevention 2020–2070. *Nature reviews Clinical oncology*, 18(10):663–672, 2021.
- [47] Zihan Sun, Yongheng Yan, Yuanhua Chen, Guorong Yao, Jiazhou Wang, Weigang Hu, Zhongjie Lu, and Senxiang Yan. A physics-informed deep learning model for predicting beam dose distribution of intensity-modulated radiation therapy treatment plans. *Physics and Imaging in Radiation Oncology*, 34:100779, 2025.
- [48] Stéphane Terry, Agnete ST Engelsen, Stéphanie Buart, Walid Shaaban Elsayed, Goutham Hassan Venkatesh, and Salem Chouaib. Hypoxia-driven intratumor heterogeneity and immune evasion. *Cancer letters*, 492:1–10, 2020.
- [49] Ray Zirui Zhang, Ivan Ezhov, Michal Balcerak, Andy Zhu, Benedikt Wiestler, Bjoern Menze, and John S Lowengrub. Personalized predictions of glioblastoma infiltration: Mathematical models, physics-informed neural networks and multimodal scans. *Medical Image Analysis*, 101:103423, 2025.
- [50] Yunjie Zhang, Ziqing Tang, Yidan Shao, Xiaoli Yue, Yifan Chu, and Dengyu Chen. Attenuated salmonella typhimurium I forms suppress tumor growth and promote apoptosis in murine ovarian tumors. *Scientific Reports*, 14(1):16045, 2024.